

CONFINEMENT OF THE SUN'S INTERIOR MAGNETIC FIELD

TOBY S. WOOD AND MICHAEL E. MCINTYRE

Department of Applied Mathematics and Theoretical Physics, University of Cambridge

T.S.Wood@damtp.cam.ac.uk

Submitted to the *Astrophysical Journal*, 21 February 2010

ABSTRACT

The simplest interior magnetic field \mathbf{B}_i that can explain the observed uniform rotation of the Sun's radiative envelope is an axial dipole stabilized by a deep toroidal field. It can explain the uniform rotation only if confined in the polar caps. The field must be prevented from diffusing up into the high-latitude convection zone, whose slower rotation must remain decoupled from the interior. This paper presents new analytical and numerical solutions showing that such confinement and decoupling is dynamically possible, by means of a laminar “magnetic confinement layer” at the bottom of the tachocline. With realistic values of the microscopic diffusivities, a weak laminar downwelling flow $U \sim 10^{-5} \text{ cm s}^{-1}$ over the poles is enough to enforce exponential decay of $|\mathbf{B}_i|$ with altitude, in a confinement layer only a fraction of a megameter thick. The reality of downwelling in the polar tachocline is implied by helioseismic observations, taken together with elementary dynamics. Our confinement-layer solutions are the first to take account of all the relevant physical effects in a self-consistent mathematical model. The effects include magnetic diffusion, baroclinicity and stable stratification (thermal and compositional), Coriolis effects, and thermal relaxation. All these effects have essential roles in the dynamics. The flow is magnetostrophic to excellent approximation. We hypothesize how the confinement layers at each pole might fit into a global dynamical picture of the solar tachocline. That picture, in turn, suggests a new insight into the lithium depletion problem.

Subject headings: MHD — Sun: abundances — Sun: interior — Sun: magnetic fields — Sun: rotation

1. INTRODUCTION

There is increasing evidence that a purely hydrodynamic theory of the solar tachocline will not work (e.g., Gough & McIntyre 1998, hereafter GM98). It seems clear that a global-scale interior magnetic field \mathbf{B}_i must be involved as well as Coriolis effects, stable stratification, baroclinicity, and thermal relaxation. In order to describe a realistically thin tachocline under dynamical conditions resembling those in today's Sun, it is crucial to take account of angular momentum transport by global-scale Maxwell stresses as well as by mean meridional circulations (MMCs).

The first attempt at a tachocline theory was that of Spiegel & Zahn (1992). It included all of

the above effects except \mathbf{B}_i . Rüdiger & Kitchatinov (1997) included \mathbf{B}_i but omitted the other effects. The first attempt to include all of them was that of GM98, in a line of investigation further developed by Garaud & Garaud (2008). Meanwhile, the dynamical importance of compositional as well as thermal stratification (e.g., Mestel 1953) was suggested for tachocline theories (McIntyre 2007). In particular, the helium settling layer beneath the tachocline is nearly impermeable to MMCs because of the small diffusivity of helium through hydrogen. This near-impermeability of compositionally stratified regions has been called the “ μ -choke” (Mestel & Moss 1986). The reality of the helium settling layer is strongly indicated both by standard solar-evolution models and by

helioseismology (e.g., Christensen-Dalsgaard et al. 1993; Ciacio et al. 1997; Elliott & Gough 1999; Christensen-Dalsgaard & Thompson 2007).¹

The need for the interior field \mathbf{B}_i arises from a well known difficulty with purely hydrodynamic theories. They tend to spread the strong differential rotation of the convection zone down into the radiative interior. This is a robust and well-understood consequence of thermal relaxation, interacting with Coriolis effects via MMCs (Haynes et al. 1991; Spiegel & Zahn 1992; Elliott 1997; McIntyre 2007; Garaud & Brummell 2008). To counter this downward spreading or burrowing tendency, angular momentum has to be transported somehow from the low-latitude tachocline to the high-latitude tachocline. The horizontal eddy viscosity proposed for this purpose by Spiegel & Zahn is inconsistent with the properties of stratified turbulence known from many studies of the terrestrial atmosphere and oceans (e.g., McIntyre 1994, 2007, & refs.). Radial transport by internal gravity waves is a physically possible alternative (e.g., Schatzman 1993; Zahn et al. 1997; Rogers & Glatzmaier 2006; Charbonnel & Talon 2007, & refs.), but overwhelmingly improbable as the main mechanism since it has no natural tendency to produce the observed uniform interior rotation.

A suitably-shaped magnetic field can, by contrast, naturally produce the required angular momentum transport, as is well known. Figure 1 is a sketch suggesting the simplest possible time-averaged field shape in the tachocline. The inner light-gray sphere marks the top of the helium settling layer. The interior beneath, not shown, contains a global-scale dipole stabilized by a deep toroidal field (e.g., Braithwaite & Spruit 2004). The inflected curves show schematically some of the time-averaged \mathbf{B} lines, as they diffuse out through the helium settling layer and encounter the shear in the tachocline.

The time averaging conceals fast processes, including the 22-year dynamo cycle, convective overshoot, and other turbulent processes. We presume that the net effect of the fast processes is qualitatively like that of a turbulent magnetic diffusivity that stops the field being wound up arbitrarily tightly by the shear. We presume furthermore that, away from the poles, the field

is held approximately horizontal by downward “magnetic flux pumping” in the overshoot layer. Though not fully understood, the effectiveness of such pumping in the overshoot layer can be strongly argued from several lines of evidence, including three-dimensional direct numerical simulations, with varying emphasis on the role of turbulent anisotropy and of vertical gradients of density and turbulent intensity (e.g., Tobias et al. 2001; Kitchatinov & Rüdiger 2008, & refs.) (see also §3 of Weiss et al. 2004, for a historical review). The shapes of the time-averaged \mathbf{B} lines in Fig. 1 are evidently such as to transport angular momentum from low to high latitudes by means of persistent Alfvénic torques.

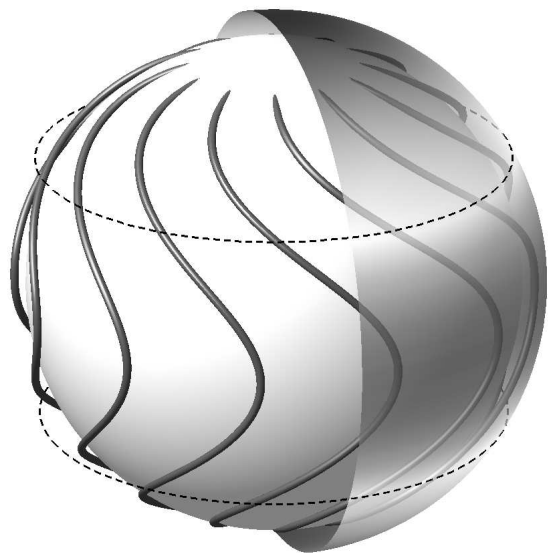


Fig. 1.— Sketch of the time-averaged magnetic field in the tachocline. Poloidal magnetic field lines emerge from the helium settling layer (inner sphere) in high latitudes, and are wound up by differential rotation in the tachocline, acting against eddy diffusion. A prograde torque is transmitted from low to high latitudes along these field lines. The slow polar and fast equatorial rotation are indicated by darker shading of the outer sphere, which represents the bottom of the convection zone. The dashed lines indicate the latitudes at which the rotation of the convection zone matches that of the interior, $\Omega_i = 2.7 \times 10^{-6} \text{s}^{-1}$.

Near the poles it is less clear that magnetic flux pumping will be effective. However, as mentioned in GM98, there are good reasons (§2 below) to expect the tachocline’s MMC near the poles to take the form of weak but persistent downwelling. This suggests that the field can be confined in the

¹Also Christensen-Dalsgaard & Gough, in preparation.

polar caps through a laminar advective–diffusive balance, the kind of balance proposed in GM98. That such confinement is possible — taking account of all the abovementioned dynamical ingredients, including strong Coriolis effects — was first shown in detail by the present authors (Wood & McIntyre 2007, hereafter WM07) by solving the relevant nonlinear equations in the limit of strong stable stratification. The solutions are “analytical” in the sense that the fields are obtained explicitly, as indefinite integrals, after first solving a linear second order ordinary differential equation for the vertical component of \mathbf{B} . The steady, magnetically diffusive, inviscid flow thus described (see Fig. 2) was called a “magnetic confinement layer”.

Apart from the fully consistent dynamics, the distinctive feature of these analytical confinement-layer solutions — contrasting with published numerical solutions that seem to argue against polar confinement (e.g., Brun & Zahn 2006) — was the ability to use realistically small values of the microscopic magnetic and thermal diffusivities. However, in WM07 we assumed that the angular momentum balance in the polar cap would include a retrograde Alfvénic torque exerted downward on the helium settling layer beneath. We now recognize this to be inconsistent with the global picture suggested in Fig. 1, though it could be made consistent, topologically at least, with the next simplest picture involving a quadrupolar interior field (see footnote 3 below). Here we focus on the simplest, dipolar picture.

The present paper therefore (a) derives alternative analytical confinement-layer solutions consistent with Fig. 1, with all the Alfvénic torque exerted sideways, (b) generalizes the solutions, using a numerical code, to allow for finite thermal and compositional stratifications, and (c) describes more fully the effects of the compositional stratification by taking account of helium advection and diffusion.

In WM07 we took both the viscosity and the helium diffusivity to be zero, allowing a finite horizontal slip velocity at the top of the helium settling layer and slight kinks in the magnetic field lines there. We conjectured that with small but finite viscosity and helium diffusivity the slip discontinuity would resolve into an Ekman layer. However, the solutions presented here will show that, instead, there is a thin “helium sublayer” mark-

ing the bottom of the confinement layer and the top of the helium settling layer (again see Fig. 2). The helium sublayer is thin by comparison with the overlying confinement layer but thick by comparison with an Ekman layer. This is because helium diffusion has more time to act against advection than viscosity against Coriolis effects. Therefore the helium sublayer is an inviscid flow, like the confinement layer. With downwelling $U \sim 10^{-5} \text{cm s}^{-1}$ the confinement layer thickness scale $\delta \sim 0.4 \text{Mm}$, and the helium sublayer $\sim 0.06 \text{Mm}$. Both are much larger than the Ekman thickness $\sim 3 \times 10^{-5} \text{Mm}$, but much smaller than tachocline thicknesses estimated from observations. The smallest such estimate is 13Mm, from Elliott & Gough (1999).

In Fig. 2 the field is strongly confined in the sense that its strength falls off exponentially with altitude, on e -folding scales of the order of δ , which is the magnetic advection–diffusion scale based on U . However, Coriolis and magnetic-induction effects make the dynamical balances aloft significantly different from those of simple advective–diffusive balance.

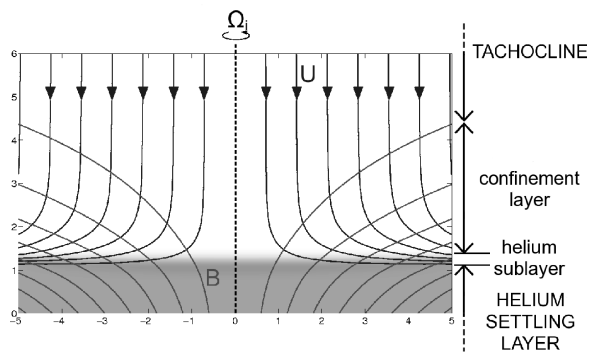


Fig. 2.— The magnetic confinement layer near the north pole. The field strength falls off exponentially with altitude. The streamlines with arrows show the downwelling responsible for the confinement. If the downwelling were switched off, the field near the pole would diffuse and become nearly vertical, as illustrated for instance in Brun & Zahn (2006). Compositional stratification is indicated by shading. With typical parameters the confinement layer is a fraction of a megameter thick. The plot is from a numerical solution; the corresponding analytical solution looks identical. The horizontal and vertical axes are colatitude r and altitude z in the dimensionless units introduced in §3.

The plan of the paper is as follows. In §2 we show that the observed differential rotation in the high-latitude tachocline does indeed imply a persistent downwelling MMC in that region. In §§3–5 we introduce the model equations and principal scalings. The equations are solved analytically in §6 and numerically in §8. The analytical solutions are made possible by assuming a self-similar horizontal structure that is asymptotically valid in the limit of strong stable stratification. This structure is self-similar in a slightly more general sense than in WM07; see equation (31) below. The resulting self-similar solutions go beyond those in WM07 in another sense as well. They describe the entire vertical structure shown in Figure 2, including the helium sublayer. In §7 we focus on scalings and dynamics in the sublayer. There, the low magnetic Reynolds number causes the momentum balance to take on the character of flow in a porous medium, as fluid pushes past the field lines. As already mentioned, true viscous effects are negligible everywhere, even in the sublayer.

The numerical solutions of §8 verify all these effects and provide additional insights. In particular, the assumption of strong stable stratification on which the self-similar solutions rely — through its consequence that the thermal and compositional stratification surfaces should be “flat”, meaning gravitationally horizontal, near the poles — is directly verified by the numerical results. They directly demonstrate the flatness by self-consistently solving the full equations, for finite stratification. The solutions allow the stratification surfaces to tilt as they may, but show that the tilt is indeed small when the stratification is realistically strong. For instance the tilt is visible in Fig. 2 only if one looks at the shading edge-on, revealing a very slight concavity.

In §9 we discuss a subtlety that arises when comparing the analytical and numerical solutions in the upper part of the flow. The dynamical balances aloft become delicate as the Lorentz and Coriolis forces become vanishingly small. The effects of truncation errors and other small effects thus complicate the comparison.

The confinement-layer theory developed in this paper concerns today’s Sun as inferred from helioseismology. But it is easily extended to cover the case of no helium settling layer. That extension provides some interesting clues about the Sun’s

early main-sequence evolution and lithium abundance, a topic to which we return in the concluding discussion, §10.

2. DOWNWELLING IN THE POLAR TACHOCLINE

The picture suggested in Figures 1 and 2 relies on the MMC pattern in the stably-stratified polar tachocline being robustly and persistently downward above the confinement layer, after averaging out any fast fluctuations due to waves and turbulence. Helioseismology provides a compelling reason to expect downwelling rather than upwelling, at least in today’s tachocline.

As is well known, the pressure, density and angular velocity fields, averaged with respect to time and longitude, robustly satisfy hydrostatic and cyclostrophic balance. Departures from such balance must take the form of fast oscillations such as p -modes and g -modes, or turbulent fluctuations. From the curl of the momentum equation we may show in the standard way that this balance implies the so-called “thermal-wind relation”. In cylindrical polar coordinates (z, r, ϕ) centered on the axis of rotation, with the axial coordinate z directed vertically upward at the north pole, the thermal-wind relation can be expressed as

$$(\nabla\rho \times \nabla P) \cdot \mathbf{e}_\phi = -r\rho^2 \frac{\partial|\boldsymbol{\Omega}|^2}{\partial z} \quad (1)$$

where $\boldsymbol{\Omega}$ is the absolute angular velocity of the Sun’s differential rotation, ρ is the density, and P is the total pressure. The unit vector \mathbf{e}_ϕ is directed azimuthally, picking out the azimuthal component of the curl; ∇P , being dominated by its hydrostatic part, is close to being vertically downward. On the assumption that the observed negative sign of $\partial|\boldsymbol{\Omega}|^2/\partial z$ persists into the region near the pole invisible to helioseismology, we must have a minimum in ρ , and hence a maximum in temperature T , on each isobaric surface at the pole.

The stably-stratified radiative envelope is a thermally relaxing system. Local temperature anomalies, defined as departures of T from local radiative equilibrium, will tend to relax back toward zero. To hold T above radiative equilibrium near the pole, there has to be persistent adiabatic compression by downwelling, with compensating upwelling and negative T anomalies in lower latitudes. The strength U of the polar downwelling is

sensitively tied to the tachocline thickness, which is not well constrained by helioseismology. GM98 estimated $U \sim 10^{-5} \text{ cm s}^{-1}$. However, our solutions will show that polar field confinement is robust over a wide range of U values, spanning several decimal orders of magnitude.

In this picture the downwelling ventilates the polar tachocline on timescales $\lesssim 10^{-1} \text{ Gyr}$, holding it compositionally unstratified as well as free of large-scale, time-averaged magnetic fields. To that extent it is like the picture put forward in GM98 and further explored in Elliott & Gough (1999), as distinct from the picture of a much deeper and less well ventilated tachocline considered in McIntyre (2007).

3. THE MODEL EQUATIONS

The aim is to model the magnetic confinement layer in a neighborhood of the north pole. We work in a frame rotating with the same angular velocity as the interior, $\Omega_i = 2.7 \times 10^{-6} \text{ s}^{-1}$, and seek axisymmetric solutions of the Boussinesq MHD equations within a cylindrical volume V surrounding the pole. The geometry of the domain is that indicated in Fig. 2. The Boussinesq approximation should be highly accurate because Mach numbers are tiny and because layer thicknesses of the order of a fraction of a megameter are far smaller than the pressure scale height, 60 Mm. In the Boussinesq equations, the distinction between temperature and potential temperature becomes immaterial.

We impose uniform downwelling of magnitude U through the top of the domain, and an axial dipolar magnetic field structure underneath to represent the interior magnetic field \mathbf{B}_i . The thickness scale for the confinement layer is the magnetic advection–diffusion scale $\delta = \eta/U$, where the magnetic diffusivity $\eta \approx 4.1 \times 10^2 \text{ cm}^2 \text{ s}^{-1}$ (Gough 2007). This gives $\delta \approx 0.4 \text{ Mm}$ if $U \approx 10^{-5} \text{ cm s}^{-1}$, as already noted.

We nondimensionalize the Boussinesq equations using δ as the lengthscale, U as the scale for the velocity field \mathbf{u} , and δ/U as the timescale, $\sim 10^5 \text{ yr}$ if $U \sim 10^{-5} \text{ cm s}^{-1}$. We measure the magnetic field \mathbf{B} in units of Alfvén speed, 0.6 cm s^{-1} per gauss at a tachocline density of 0.2 g cm^{-3} , and nondimensionalize \mathbf{B} with respect to $(2\Omega_i\eta)^{1/2} \approx 0.05 \text{ cm s}^{-1}$. The significance of

this scaling will be explained in §5. We suppose that the thermal and compositional stratifications are approximately uniform within the helium settling layer, shaded in Fig. 2. Writing \hat{T} and $\hat{\mu}$ for the fractional perturbations of temperature and mean molecular weight, we define the buoyancy frequencies N_T and N_μ to be exactly constant at the bottom of the domain,

$$\left. \frac{\partial \hat{T}}{\partial z} \right|_{\text{bottom}} = \frac{N_T^2 \delta}{g} = \text{const.}, \quad (2)$$

$$\left. \frac{\partial \hat{\mu}}{\partial z} \right|_{\text{bottom}} = -\frac{N_\mu^2 \delta}{g} = \text{const.}, \quad (3)$$

where z is now the dimensionless axial or altitude coordinate. At the top of the helium settling layer we have $N_T \approx 0.8 \times 10^{-3} \text{ s}^{-1}$ (Gough 2007), and $N_\mu \approx 0.5 \times 10^{-3} \text{ s}^{-1}$ (e.g., Christensen-Dalsgaard & Thompson 2007).² In place of \hat{T} and $\hat{\mu}$ we define dimensionless rescaled quantities T and μ by

$$\frac{N_T^2 \delta}{g} T = \hat{T}, \quad (4)$$

$$\frac{N_\mu^2 \delta}{g} \mu = \hat{\mu}. \quad (5)$$

The thermal and compositional diffusivities are denoted respectively by $\kappa \approx 1.4 \times 10^7 \text{ cm}^2 \text{ s}^{-1}$ and $\chi \approx 0.9 \times 10^1 \text{ cm}^2 \text{ s}^{-1}$ (Gough 2007). We then arrive at the following dimensionless Boussinesq equations,

$$\text{Ro} \frac{D\mathbf{u}}{Dt} + \mathbf{e}_z \times \mathbf{u} = -\nabla p + \alpha_T T \mathbf{e}_z - \alpha_\mu \mu \mathbf{e}_z + (\nabla \times \mathbf{B}) \times \mathbf{B} + \text{Ek} \nabla^2 \mathbf{u} \quad (6)$$

$$0 = \nabla \cdot \mathbf{u} \quad (7)$$

$$\frac{\partial \mathbf{B}}{\partial t} = \nabla \times (\mathbf{u} \times \mathbf{B}) + \nabla^2 \mathbf{B} \quad (8)$$

$$0 = \nabla \cdot \mathbf{B} \quad (9)$$

$$\frac{DT}{Dt} = \frac{\kappa}{\eta} \nabla^2 T \quad (10)$$

$$\frac{D\mu}{Dt} = \frac{\chi}{\eta} \nabla^2 \mu \quad (11)$$

²Estimates of N_μ vary (e.g., Christensen-Dalsgaard et al. 1993). The value $N_\mu \approx 0.5 \times 10^{-3} \text{ s}^{-1}$ was computed in McIntyre (2007, §8.5) from information given in Christensen-Dalsgaard & Thompson (2007). However, the work presented in this paper depends only on N_μ having an order of magnitude similar to N_T , which is consistent with all the estimates we have seen.

where $D/Dt = \partial/\partial t + \mathbf{u} \cdot \nabla$, the Lagrangian or material derivative, and where \mathbf{e}_z is the unit vector parallel to the rotation axis. We have defined four dimensionless coefficients Ro, Ek, and

$$\alpha_T = \frac{N_T^2 \delta^2}{2\Omega_i \eta}, \quad \alpha_\mu = \frac{N_\mu^2 \delta^2}{2\Omega_i \eta}; \quad (12)$$

Ro and Ek are Rossby and Ekman numbers defined by

$$\text{Ro} = \frac{U/\delta}{2\Omega_i}, \quad \text{Ek} = \frac{\nu}{2\Omega_i \delta^2} = \frac{\nu}{\eta} \text{Ro} \quad (13)$$

where ν is the kinematic viscosity, the sum of molecular and radiative contributions, $\approx 2.7 \times 10^1 \text{cm}^2 \text{s}^{-1}$ (Gough 2007). In (11) we have neglected gravitational settling, an excellent approximation in virtue of the short timescale of the confinement-layer dynamics relative to the Sun's lifetime.

For $U \sim 10^{-5} \text{cm s}^{-1}$ the Rossby number is tiny, $\text{Ro} \sim 0.5 \times 10^{-7}$, and the Ekman number is smaller still, because $\nu/\eta \approx 0.7 \times 10^{-1}$. To excellent approximation, therefore, the flows under consideration will be magnetostrophic. In (6) the Coriolis force will be balanced against the combined pressure-gradient, buoyancy, and Lorentz forces:

$$\mathbf{e}_z \times \mathbf{u} = -\nabla p + \alpha_T T \mathbf{e}_z - \alpha_\mu \mu \mathbf{e}_z + (\nabla \times \mathbf{B}) \times \mathbf{B}. \quad (14)$$

We are concerned here only with axisymmetric steady states. Then the azimuthal components of (14) and its curl are respectively

$$u_r = \frac{1}{r} \mathbf{B} \cdot \nabla (r B_\phi), \quad (15)$$

$$\frac{\partial u_\phi}{\partial z} = \alpha_T \frac{\partial T}{\partial r} - \alpha_\mu \frac{\partial \mu}{\partial r} + \frac{1}{r} \frac{\partial}{\partial z} (B_\phi^2) - r \mathbf{B} \cdot \nabla \left(\frac{[\nabla \times \mathbf{B}]_\phi}{r} \right) \quad (16)$$

where r is the dimensionless perpendicular distance from the rotation axis, and where suffixes denote vector components.

Equation (15) represents the local torque balance about the rotation axis, after multiplication by r . It describes how the retrograde Coriolis torque from the equatorward flow is balanced by the prograde Lorentz torque from the confined magnetic field. Equation (16) represents

low Rossby number thermal-wind balance generalized to include compositional gradients and the Lorentz force-curl, as contrasted with the standard thermal-wind balance, equation (1), that applies above the confinement layer.

Although the balances (15)–(16) are keys to physical understanding, for numerical solution it proves more expedient to use the full equations (6)–(11). Directly imposing magnetostrophic balance causes numerical ill-conditionedness, for reasons discussed in Appendix C.

4. BOUNDARY CONDITIONS

We need to specify boundary conditions or equivalent information. This inevitably involves artificial choices. The only way to avoid making such choices would be to fit the polar caps into the complete, and highly complicated, global picture. Given the limitations of current computing resources, there is no known way to construct a global solution with realistic microscopic values of η , κ , χ , and ν in the polar confinement layers, and realistic three-dimensional models of turbulence and magnetic flux pumping in lower latitudes.

As already noted, we are imposing a dipolar magnetic field structure underneath the confinement layer, with vanishing Alfvénic torque, and a uniform downwelling of magnitude U from a field-free region aloft. Field-free refers to time-averaged fields. For the analytical solutions “aloft” means $z \rightarrow +\infty$, and for the numerical solutions it means a dimensional altitude $\approx 6\delta$ above the helium sub-layer. Dimensionlessly, 6δ corresponds to $z = 6$ and downwelling U corresponds to $u_z = -1$.

It will prove possible to find solutions both with and without vertical shear $\partial u_\phi / \partial z$ aloft. The corresponding temperature boundary conditions must take account of (16). Their full specification is left open at this stage because in reality it depends on completion of the global picture, including solution of the perturbed global-scale heat flow problem and a match to $\partial u_\phi / \partial z$ in the overlying bulk of the stably-stratified tachocline, be it laminar or, more likely, MHD-turbulent (e.g., Spruit 2002; Parfrey & Menou 2007, & refs.). Fortunately, for reasons to emerge in the next two sections, our solutions turn out to have no critical dependence on the temperature boundary conditions aloft and beneath, beyond compatibility with

(16) and with the stable stratification.

At the periphery of the domain, an artificial cylindrical surface $r = r_d$, say, the numerical algorithm requires us to specify three vertical profiles, including the vertical profile of Maxwell stress. The stress profile represents the field lines' connection to lower latitudes and the Alfvénic torque exerted therefrom. We also need to specify the thermal and compositional stratification profiles $T(z)$ and $\mu(z)$ at the periphery, in a manner consistent with scalings in the confinement layer and helium sublayer (§§5, 7). In this way we artificially fix the altitude of the helium sublayer. We thereby influence the velocity field as well, since it is tightly linked to the two stratifications by equations (10) and (11). The velocity field, especially the azimuthal component u_ϕ , is also influenced by the Maxwell stress profile, as will be described in §8.

For the numerical solutions the bottom boundary is at depth $\approx \delta$ beneath the helium sublayer, i.e., at $z \approx -1$. On the bottom we impose the conditions (2) and (3), equivalently $\partial T/\partial z = 1$ and $\partial \mu/\partial z = -1$. We also impose $u_\phi = 0$, i.e., that the interior has no differential rotation, as expected from the global picture. We then make iterative adjustments to the Maxwell stress profile at the periphery, so as to approach zero Alfvénic torque at each r on the bottom, in the steady state, equivalent to $B_\phi = 0$ on the bottom.

For the analytical solutions there is slightly less freedom in the boundary conditions, again for reasons to emerge in the next two sections. It is possible to specify at most two peripheral vertical profiles, for instance the Maxwell stress profile or the $B_\phi(z)$ profile, together with one or other of $T(z)$ or downwelling $u_z(z)$. Or, as the numerical procedure suggests, instead of specifying the peripheral B_ϕ profile we may specify the radial, i.e., colatitudinal, profile of B_ϕ on the bottom. The radial and peripheral profiles are equivalent because of the Alfvénic coupling between bottom and periphery evident in Fig. 2, and expressed mathematically by the $\mathbf{B} \cdot \nabla$ operator in equation (15). Since we want solutions with vanishing bottom torque we specify $B_\phi \rightarrow 0$ as $z \rightarrow -\infty$. As shown in §6, the corresponding peripheral stress profile can then be computed analytically, without iteration, thanks to the self-similar horizontal structure of the analytical solutions.

The overall torque balance for the confinement

layer can be expressed by integrating r times (15) over the volume V of the cylindrical domain, then using the divergence theorem. With the foregoing boundary conditions, the result is

$$\int_{\partial V} \frac{1}{2} r^2 \mathbf{u} \cdot d\mathbf{S} = r_d \int_{\partial V} B_\phi \mathbf{B} \cdot d\mathbf{S} \quad (17)$$

where $d\mathbf{S}$ is the vector area element directed outward. The boundary conditions imply that the domain boundary ∂V on the right-hand side of (17) can be taken as the periphery only, allowing the moment arm $r = r_d$ to be taken outside the integral. The boundary conditions also imply that ∂V on the left-hand side of (17) can be taken as the top and periphery only. In the corresponding dimensional equation, $\frac{1}{2} r^2$ is replaced by $\Omega_i r^2$, the absolute angular momentum per unit mass after neglecting contributions $O(\text{Ro})$.

The right-hand side of (17) can be recognized as r_d times the integrated Maxwell stress profile, which is equal to total Alfvénic torque exerted on the confinement layer from the periphery. The left-hand side represents the net rate of absolute angular momentum export by the MMC coming in through the top and out through the periphery. It is positive for any velocity field qualitatively like that in Fig. 2. The Alfvénic torque must therefore also be positive, i.e., prograde. The boundary conditions ensure that this torque comes exclusively from the confinement layer's sideways connection to low latitudes,³ via field lines like those sketched in Fig. 1; see also Fig. 4 below.

5. CONFINEMENT-LAYER SCALINGS

Consider the scaling regime above the helium sublayer. Because the photon mean free path makes the thermal diffusivity relatively large, $\kappa/\eta \sim 3 \times 10^4$, the confinement-layer flow only weakly perturbs the background thermal stratification. Consistently with (2) and (4) we define

³If the global-scale poloidal field had been assumed to have a quadrupolar rather than dipolar structure, then part of the torque could have been transmitted from low to high latitudes via the deep radiative interior as well. In this work we consider only the simpler, dipolar case in which all the torque is transmitted horizontally, as suggested in Fig. 1. This is consistent with our boundary condition $B_\phi \rightarrow 0$ beneath the confinement layer. Of course there must still be a nonvanishing B_ϕ component deeper within the interior, in order to stabilize the neutral ring of the dipolar field (e.g., Braithwaite & Spruit 2004).

$T = z + \text{const.} + T'$. Then, sufficiently close to the pole, the leading-order balance in the steady-state thermal equation (10) involves only the vertical component u_z of \mathbf{u} ,

$$u_z = \frac{\kappa}{\eta} \nabla^2 T'. \quad (18)$$

From this we estimate the magnitude of the thermal anomaly to be $T' \sim \eta/\kappa \ll 1$. By contrast, the diffusivity of helium is relatively small, $\chi/\eta \approx 2 \times 10^{-2}$, so the diffusive flux of helium up into the bulk of the confinement layer is negligible. The confinement layer is therefore well ventilated, i.e., the mean molecular weight μ within the bulk of the confinement layer is close to being constant. Compositional stratification is important only in the helium sublayer and the helium settling layer, as indicated by the shading in Fig. 2 and further discussed in §7.

The generalized thermal-wind equation (16) describes how the Coriolis and Lorentz azimuthal force-curves act to tilt the stratification surfaces. If the thermal stratification N_T is sufficiently strong, i.e., α_T sufficiently large, then the tilting will be only slight. In the asymptotic limit $\alpha_T \rightarrow \infty$ the thermal stratification surfaces will become perfectly flat.

The degree of flatness will now be estimated from (16) using scaling arguments. The vertical component B_z of \mathbf{B} will play a central role. Let \mathbf{B} be the dimensional magnitude of B_z at the bottom of the confinement layer, in units of Alfvén speed. Then the dimensionless magnitude of B_z is $\Lambda^{1/2}$, where

$$\Lambda = \frac{\mathbf{B}^2}{2\Omega_i \eta}, \quad (19)$$

the Elsasser number based on \mathbf{B} .

The degree of flatness cannot be uniform in r . Sufficiently near the pole we expect that the horizontal components of \mathbf{u} and \mathbf{B} will all be proportional to r , as will be verified in §6. Then (16) shows that $\partial T/\partial r = \partial T'/\partial r \propto r$ so that, on the assumption of smooth behavior near the pole, T' must have the form

$$T' = a_T + \frac{1}{2} b_T r^2 \quad (20)$$

where a_T and b_T are functions of z alone. As already noted from (18), $a_T \sim \eta/\kappa \ll 1$. The magnitude of b_T is governed by (16). We may therefore

deduce from (16) the radius or colatitudinal distance within which it is valid to regard the thermal stratification surfaces as flat, to a self-consistent approximation. For realistic solar parameters, this radius of validity will shortly be seen to be quite large, in some cases larger than R_\odot .

The order-of-magnitude condition for approximate flatness is $b_T r^2 \ll a_T$, or $r^2 \ll r_T^2$, say, where r_T denotes a typical magnitude of $|a_T/b_T|^{1/2}$, a dimensionless number. More precisely, $r^2 \ll r_T^2$ is the condition for validity of any solution with approximately uniform downwelling and approximately flat thermal stratification surfaces, compatible with (18).

We estimate b_T and r_T from (16) on the assumption that the near-pole behavior of the fields correctly indicates orders of magnitude not only for $r \ll r_T$ but also out as far as $r \sim r_T$. From this assumption, and from axisymmetry and from the conditions (7) and (9) that \mathbf{u} and \mathbf{B} are divergence-free, we expect that at all $r \lesssim r_T$ the radial, i.e., colatitudinal, components of \mathbf{u} and \mathbf{B} are typically larger than the vertical components by a factor r . Also using (15) and the azimuthal component of (8), and assuming $\partial/\partial z \sim 1$ and $\partial/\partial r \sim r^{-1}$, we find that the dimensionless magnitudes satisfy

$$u_z \sim 1 \quad (21)$$

$$u_r \sim r \quad (22)$$

$$u_\phi \sim r\Lambda^{-1} \quad (23)$$

$$B_z \sim \Lambda^{1/2} \quad (24)$$

$$B_r \sim r\Lambda^{1/2} \quad (25)$$

$$B_\phi \sim r\Lambda^{-1/2} \quad (26)$$

for all $r \lesssim r_T$. These relations can be explicitly checked using the self-similar solutions presented in §6. For increasing values of Λ the field lines become stiffer, so that both they and the velocity streamlines spiral less tightly, as noted in WM07. The magnitude of Λ is not well constrained by observations, depending as it does on the magnitude of the interior field at the top of the radiative envelope. Fortunately, it will be found that the confinement-layer regime described here can accommodate a considerable range of Λ values.

In (16), with the term in α_μ neglected, the term in α_T cannot exceed the largest of the other terms in order of magnitude. Assuming that the order-

of-magnitude relation $\partial T'/\partial r \sim b_T r$ applies out as far as $r \sim r_T$, we see that the term in α_T has magnitude $\sim \alpha_T b_T r$ at all $r \lesssim r_T$. The remaining terms in (16) have magnitudes either $\sim r\Lambda^{-1}$ (the terms in u_ϕ and B_ϕ^2) or $\sim r\Lambda$ (the last term). These magnitudes follow from (21)–(26) along with our assumptions $\partial/\partial z \sim 1$ and $\partial/\partial r \sim r^{-1}$. We may therefore define the typical magnitude of b_T to be $\alpha_T^{-1} \max(\Lambda, \Lambda^{-1})$. Correspondingly, with $a_T \sim \eta/\kappa$ and $\alpha_T = N_T^2 \delta^2 / 2\Omega_i \eta$ we may define r_T^2 , the typical magnitude of a_T/b_T , as $\alpha_T(\eta/\kappa) \min(\Lambda, \Lambda^{-1})$, i.e., as

$$r_T^2 = \frac{N_T^2 \delta^2}{2\Omega_i \kappa} \min(\Lambda, \Lambda^{-1}). \quad (27)$$

For realistic $N_T \approx 0.8 \times 10^{-3} \text{s}^{-1}$, for downwelling $U \approx 10^{-5} \text{cm s}^{-1}$, and for $\Lambda \sim 1$, we have $r_T \sim 4 \times 10^3$. With these numbers, which imply $\delta \sim 0.4 \text{Mm}$, the dimensional colatitudinal distance at which the tilting of the thermal stratification surfaces can become significant is $r_T \delta \approx 1600 \text{Mm}$, more than $2R_\odot$ away from the pole.⁴ The validity of the foregoing scale analysis will be independently checked by the numerical solutions in §8.

Of course our cylindrical model with its assumption of uniform downwelling will itself cease to apply, almost certainly, before we get as far as $r_T \delta$ from the pole. At some colatitude the downwelling must give way to upwelling. The confinement-layer regime cannot then apply even qualitatively. Instead, the interior magnetic field lines are free to advect and diffuse upward until they encounter the magnetic flux pumping associated with the convective overshoot layer, as assumed in Fig. 1. This has wider implications to be discussed in §10, including implications for lithium burning.

With $\Lambda \sim 1$ and the other numbers just given, the interior field \mathbf{B}_i has dimensional orders of magnitude typified by $B_{ir} \sim 30 \text{cm s}^{-1}$, equivalently

⁴Even when the tilting is significant, the slopes of the thermal stratification surfaces are far smaller than the geometrical aspect ratio r_T^{-1} . Indeed, on a global scale we expect the stratification surfaces to depart from the horizontal by only “a very tiny fraction of a megametre” from pole to equator (McIntyre 2007, end of §8.5), based on observational constraints on shear in the tachocline. Here, as always in dynamics, “horizontal” has the same meaning as in snooker, namely tangential to the heliopotentials including both the centrifugal and the gravitational potential.

50G, at colatitude $\sim 30^\circ$, or a third of those values at colatitude $\sim 10^\circ$. Such $|\mathbf{B}_i|$ values are far above the threshold, more like 10^{-2}G , for the field strength required to enforce the Ferraro constraint in the interior (e.g., Mestel & Weiss 1987; Charbonneau & MacGregor 1993). However, a separate question beyond the scope of this study concerns the possible range of field strengths, and MHD turbulent intensities in the bulk of the tachocline, required to support the time-averaged picture suggested in Fig. 1. There, field strengths greater than 10^{-2}G might well be needed.

The range of interior field strengths accommodated by the confinement-layer regime is determined by (27). The condition for the regime to apply at least qualitatively within, say, 10° colatitude of the poles is $r_T \delta \gtrsim 90 \text{Mm}$. We can use (27) together with realistic N_T and diffusivity values to write this condition as

$$\max(\Lambda, \Lambda^{-1}) \lesssim 3 \times 10^2 \left(\frac{U}{10^{-5} \text{cm s}^{-1}} \right)^{-4}. \quad (28)$$

So for $U \sim 10^{-5} \text{cm s}^{-1}$ the regime applies over a range of about five decimal orders of magnitude in Λ . If the downwelling is weaker then a much wider range of Λ values may become possible.

6. THE ANALYTICAL SOLUTIONS

We now assume perfect flatness, $r_T \rightarrow \infty$. We also assume $N_\mu \sim N_T$ within and beneath the helium sublayer, as is realistic for today’s Sun. Then not only the thermal but also the compositional stratification surfaces are flat. Scalings and dynamics in the sublayer are discussed in §7, where it will be shown that our flatness assumptions are justified even more strongly than in the bulk of the confinement layer.

Perfect flatness requires that the steady-state poloidal velocity field is self-similar in a simple sense. Its vertical component u_z has no horizontal variation — the downwelling must be uniform everywhere — and its horizontal component $u_r \propto r$. This follows from equations (7), (10) and (11) and the steady-state assumption $\partial/\partial t = 0$. The induction equation (8) and the steady-state assumption then permit a poloidal magnetic field that is also

self-similar. The resulting equations are

$$ru_r = \mathbf{B} \cdot \nabla (rB_\phi) \quad (29)$$

$$0 = \frac{1}{r} \frac{\partial (ru_r)}{\partial r} + \frac{du_z}{dz} \quad (30)$$

$$r\mathbf{u} \cdot \nabla \frac{B_\phi}{r} = r\mathbf{B} \cdot \nabla \frac{u_\phi}{r} + \left(\nabla^2 - \frac{1}{r^2} \right) B_\phi \quad (31)$$

$$u_z \frac{dB_z}{dz} = B_z \frac{du_z}{dz} + \frac{d^2 B_z}{dz^2} \quad (32)$$

$$0 = \frac{1}{r} \frac{\partial (rB_r)}{\partial r} + \frac{dB_z}{dz} . \quad (33)$$

Perfect flatness implies that the meridional components of (6), equivalently (16), are not needed. The azimuthal component is taken as (15) and multiplied by r to give (29), expressing the balance between Coriolis and Lorentz torques as before. Equations (30)–(33) correspond to (7)–(9); (10) and (11) have no further dynamical role. Equation (31) permits more general toroidal magnetic and differential-rotation fields than were considered in WM07, hence more freedom in the boundary conditions.

The radial components of \mathbf{u} and \mathbf{B} can be found directly from their vertical components using (30) and (33):

$$u_r = -\frac{r}{2} \frac{du_z}{dz} , \quad (34)$$

$$B_r = -\frac{r}{2} \frac{dB_z}{dz} . \quad (35)$$

As noted in §4, we are free at this stage to specify two boundary profiles. For instance we may specify the Maxwell stress profile and the downwelling profile $u_z(z)$. It is convenient to specify $u_z(z)$ first. Because of the self-similar structure, this fixes the entire poloidal velocity field. With no further information we can then find $B_z(z)$ immediately, by solving the vertical component (32) of the induction equation as a linear ordinary differential equation. The boundary conditions imply that B_z vanishes far above the confinement layer ($z \rightarrow +\infty$) and matches on to the interior field \mathbf{B}_i beneath the confinement layer ($z \rightarrow -\infty$). This matching fixes the value of \mathbf{B} and therefore of Λ . We suppose that \mathbf{B}_i has a simple, fully diffused dipolar structure, with components satisfying $B_{i\phi} = 0$, $B_{ir}/r = \text{constant}$, and B_{iz} a linear function of z consistent with (35). Even though the balance in (32) is not

simple advective–diffusive, we find that B_z decays upward like $\exp(-z)$.

Once we have $B_z(z)$ we can calculate B_r from (35), and then the toroidal field B_ϕ from (29) by using (34) and taking advantage of the hyperbolic character of the operator $\mathbf{B} \cdot \nabla$. By calculating B_ϕ in this way, we ensure that the Lorentz torque balances the Coriolis torque along each magnetic field line. It is here that we need to specify a second boundary profile. This can be the peripheral Maxwell stress profile or equivalently $B_\phi(z)$, at $r = r_d$, or the radial or colatitudinal profile $B_\phi(r)$ at some altitude $z = z_0$. It could also be the profile of B_ϕ on any surface of revolution intersecting the field lines. Since we want zero Alfvénic torque on the bottom, we choose to specify $B_\phi(r, z) \rightarrow 0$ for all r as $z \rightarrow -\infty$. We then have the following, unique solution of (29):

$$B_\phi = B_z \int_{-\infty}^z \frac{u_r}{B_z^2} dz . \quad (36)$$

For any u_r profile that decays exponentially downward beneath the helium sublayer (§7), this solution for B_ϕ , and with it the Maxwell stress and Alfvénic torque, will also decay exponentially downward. The expression (36) then shows that B_ϕ has the same self-similar functional form as u_r , namely r times a function of z alone.

To ensure that \mathbf{B}_ϕ decays aloft, as $z \rightarrow +\infty$, it is sufficient to assume that

$$u_r = O(\exp(-\gamma z)) \quad \text{as } z \rightarrow +\infty \quad (37)$$

where $\gamma > 1$, implying that $u_z(z) \sim -1 + O(\exp(-\gamma z))$. The three cases $\gamma > 2$, $\gamma = 2$, and $2 > \gamma > 1$ need separate consideration. When $\gamma > 2$, the only case considered in WM07, the integral in (36) converges to a constant plus $O(\exp(-(\gamma-2)z))$ as $z \rightarrow +\infty$. That in turn means that B_ϕ decays upward like $\exp(-z)$. When $\gamma = 2$, the integral in (36) asymptotes to a linear function of z , and B_ϕ decays upward like $z \exp(-z)$. When $2 > \gamma > 1$, the integral in (36) increases upward like $\exp((2-\gamma)z)$, but B_ϕ still decays upward, like $\exp(-(\gamma-1)z)$.

In all these cases it is clear from (36) that the field components B_z and B_ϕ are not exactly proportional, as they would be if they both satisfied simple advective–diffusive balance. Such proportionality would make the right-hand side of (29)

vanish, as is readily shown. Thus it is the more or less subtle *departures* from advective–diffusive balance, including the contribution to B_ϕ from the twisting of field lines by the differential rotation u_ϕ , that enable the Lorentz torque on the right of (29) to support the flow u_r at all altitudes.

The u_ϕ field that does the twisting can be calculated next, from (31) and the condition that the helium settling layer has no differential rotation, $u_\phi \rightarrow 0$ as $z \rightarrow -\infty$. Again this calculation depends on the hyperbolic character of $\mathbf{B} \cdot \nabla$. When B_ϕ is given by (36) we have, uniquely,

$$u_\phi = \int_{-\infty}^z \left(u_z \frac{\partial B_\phi}{\partial z} - \frac{\partial^2 B_\phi}{\partial z^2} \right) \frac{dz}{B_z} \quad (38)$$

showing that u_ϕ also has the form r times a function of z alone. That is, the differential rotation is shellular solid rotation. In the three cases $\gamma > 2$, $\gamma = 2$, and $2 > \gamma > 1$, the behaviors of u_ϕ as $z \rightarrow +\infty$ are respectively $u_\phi \sim \text{constant}$, $u_\phi \sim \pm z$, and $u_\phi \sim \pm \exp((2-\gamma)z)$.

Cases with negative shear aloft, $\partial u_\phi / \partial z < 0$, especially the third case, with exponentially-increasing negative shear aloft, are all suggestive of a possible way to match upwards to the observed, much stronger negative shear in the bulk of the tachocline. The sign of the shear $\partial u_\phi / \partial z$ aloft can be shown from (38) to be the same as the sign of u_r aloft, with $\partial u_\phi / \partial z \approx (\gamma-1)u_r/B_z^2$. We can therefore find self-similar solutions that match onto the tachocline shear provided that there is an exponentially weak poleward mass flux above the confinement layer. However, a more precise description of such matching may well need to take account of slight departures from magnetostrophic balance due to small-scale MHD turbulence (e.g., Parfrey & Menou 2007, & refs.), as well as slight departures from perfect flatness.

Although the structure aloft is sensitive to γ values, (36) and (38) show that, by contrast, the structure of the rest of the confinement layer is relatively insensitive. Figure 3 shows the vertical profiles of u_z , u_r/r , u_ϕ/r , B_z , B_r/r , and B_ϕ/r in a case with $\gamma = 2.24$. By construction this closely approximates the numerical example shown in Fig. 2. For other γ values the bottom half of each plot looks qualitatively the same, whereas the top half may in some cases be wildly different (see §9).

Some three-dimensional streamlines and mag-

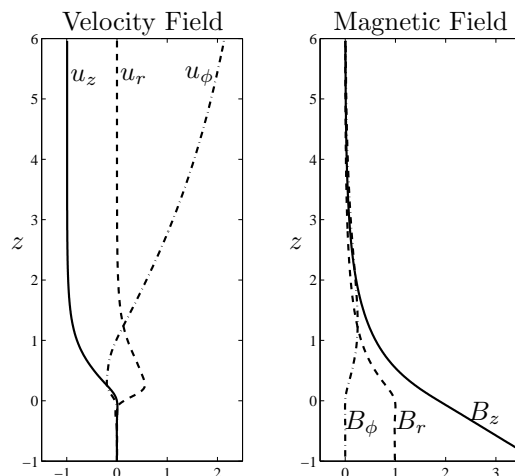


Fig. 3.— Vertical profiles from a self-similar solution of the confinement layer equations in the limit $r_T \rightarrow \infty$. The downwelling profile $u_z(z)$, solid curve on left, was chosen to match the downwelling profile from a numerical solution with $r_T^2 \approx 14$ (see §8). For numerical reasons, small adjustments were made to this profile in the “slippery” region $z > 1.5\delta$ (see §9). In (37) the decay constant $\gamma = 2.24$, and the u_ϕ profile therefore approaches a constant like $\exp(-0.24z)$.

netic field lines corresponding to the solution in Fig. 3 are plotted in Fig. 4, showing how the prograde Lorentz torque on the right of (29), associated with field-line curvature, balances the retrograde Coriolis torque on the left of (29) and satisfies the overall torque balance (17).

Finally we can calculate the vertical T and μ profiles, not shown, from (10) and (11). In the perfect-flatness limit $r_T \rightarrow \infty$ these are functions of z alone and contain no further dynamical information, beyond having enforced the self-similarity of u_z and u_r at the outset. In particular, the $\mu(z)$ profile confirms that the bulk of the sublayer is well ventilated, with μ very close to a constant everywhere above $z \approx 0.5$. Between $z \approx 0.5$ and $z \approx 0.2$ the profile goes smoothly over into the constant slope characterizing the helium settling layer beneath. The $\mu(z)$ profile from the corresponding numerical solution is almost identical, providing one of several cross-checks on the integrity of the analytical and the numerical calculations.

For finite r_T the self-similar solutions will still be valid in a range of colatitudes surrounding the pole, $r \ll r_T$; recall (27) and (28). At greater

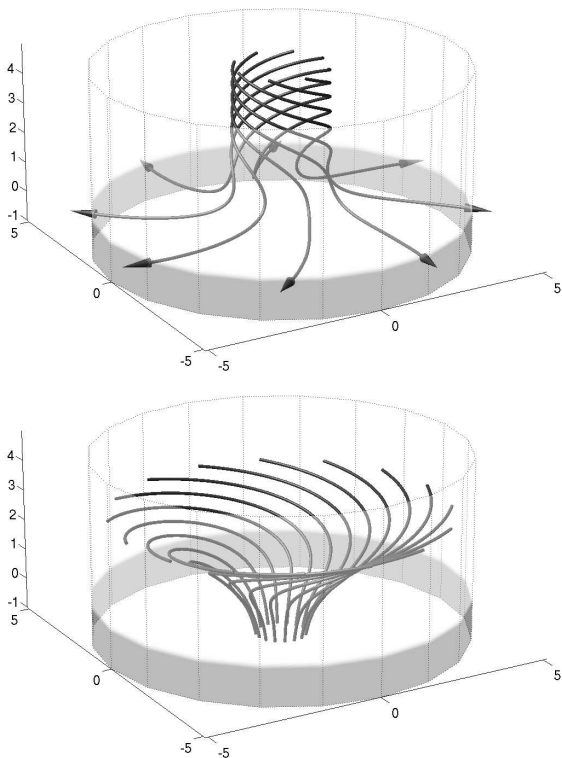


Fig. 4.— A self-similar solution of the confinement layer equations in the limit $r_T \rightarrow \infty$. The downwelling profile $u_z(z)$ was chosen to match the downwelling profile from a numerical solution with $r_T^2 \approx 14$. For numerical reasons, small adjustments were made to this profile in the “slippery” region $z > 1.5\delta$ (see §9). The peripheral shading indicates the helium settling layer and helium sublayer.

colatitudes the tilting of the thermal stratification surfaces must be supported against thermal diffusion by a non-self-similar poloidal velocity field. The scale analysis in §5 implies that the non-self-similar correction fields become comparable to those of the self-similar solution at horizontal distances $\sim r_T\delta$ from the pole.

7. THE HELIUM SUBLAYER

In order for the analytical solutions to be physically realistic, $u_z(z)$ must be chosen to be compatible with a physically realistic helium-sublayer structure whose dynamical balances fit in with our assumptions about tilting and flatness.

As just recalled, the helium sublayer marks the transition between the compositionally well-ventilated confinement layer and the nearly impermeable, compositionally stratified helium settling

layer. Therefore, we expect the dimensional sublayer thickness scale, δ_χ say, to be determined by the strain rate $\sim U/\delta$ just above the sublayer, because $u_z \rightarrow 0$ just beneath. In this situation, the operator $\mathbf{u} \cdot \nabla$ scales like the strain rate when operating on the scalar field μ in (11). The strain rate U/δ must therefore be comparable to the helium diffusion rate χ/δ_χ^2 . Since $U/\delta = \eta/\delta^2$,

$$\delta_\chi \sim (\chi/\eta)^{1/2}\delta \approx \delta/7. \quad (39)$$

For realistic solar parameters, δ_χ greatly exceeds the Ekman thickness scale $\delta_{\text{Ek}} = (\nu/2\Omega_i)^{1/2}$. Specifically,

$$\begin{aligned} \frac{\delta_\chi^2}{\delta_{\text{Ek}}^2} &\sim \frac{\chi\delta^2}{\eta} \frac{2\Omega_i}{\nu} \sim \frac{\chi\delta}{U} \frac{2\Omega_i}{\nu} \\ &\sim \frac{\chi}{\nu} \text{Ro}^{-1} \gg 1, \end{aligned} \quad (40)$$

because $\chi/\nu \approx 0.3$ while $\text{Ro}^{-1} \gg 1$, typically by many decimal orders of magnitude; recall (13). So the effects of compositional stratification dominate over viscous effects, and no Ekman layer forms.

To good approximation, therefore, the dynamics of the helium sublayer is described by the asymptotic regime

$$\delta_{\text{Ek}} \ll \delta_\chi \ll \delta. \quad (41)$$

As suggested by (39)–(40), the scale separation implied by (41) is realistic for realistic solar parameters. We therefore assume (41) throughout this section.

Under (41) the magnetic diffusion rate η/δ_χ^2 in the sublayer greatly exceeds the helium diffusion rate $\chi/\delta_\chi^2 \sim U/\delta$. The flow within the sublayer can therefore induce only a small departure $\mathbf{B} - \mathbf{B}_i = \mathbf{B}'$, say, from the interior field \mathbf{B}_i . In Figs. 2 and 4, the field lines are hardly deflected as they cross the sublayer. We therefore analyze the sublayer as a perturbation to the state with $\mathbf{u} = 0$ and $\mathbf{B} = \mathbf{B}_i$, where \mathbf{B}_i has the simple dipolar structure already assumed, with components satisfying $B_{i\phi} = 0$, $B_{ir}/r = \text{constant}$, and B_{iz} a linear function of z consistent with (35). Any such \mathbf{B}_i has $\nabla \times \mathbf{B}_i = 0$ and Lorentz force $(\nabla \times \mathbf{B}_i) \times \mathbf{B}_i = 0$. We show in Appendix A that, in the asymptotic regime given by (41), the momentum balance (14) in the sublayer becomes

$$\mathbf{e}_z \times \mathbf{u} = -\nabla \tilde{p} - \alpha_\mu \mu \mathbf{e}_z + B_{iz} \frac{\partial}{\partial z} \mathbf{B}', \quad (42)$$

and the steady-state induction equation becomes

$$0 = B_{iz} \frac{\partial}{\partial z} \mathbf{u} + \frac{\partial^2}{\partial z^2} \mathbf{B}', \quad (43)$$

in the dimensionless variables of §3. In (42), $\nabla \tilde{p}$ is a modified pressure gradient incorporating the gradient contributions to the Lorentz force and thermal buoyancy; see Appendix A, below (A3). Because $\delta_\chi \ll \delta$ and because, as verified shortly, the sublayer will prove to be even flatter than the overlying confinement layer, we may take B_{iz} to be constant throughout the sublayer. It is convenient to equate the dimensional value of this constant to B in the definition (19) of the Elsasser number Λ . Then the dimensionless magnitude of B_{iz} is precisely $\Lambda^{1/2}$. We can now integrate (43) to give

$$0 = \Lambda^{1/2} \mathbf{u} + \frac{\partial \mathbf{B}'}{\partial z} \quad (44)$$

since both \mathbf{B}' and \mathbf{u} vanish beneath the sublayer. Using (44) we write (42) as

$$\mathbf{e}_z \times \mathbf{u} = -\nabla \tilde{p} - \alpha_\mu \mu \mathbf{e}_z - \Lambda \mathbf{u}. \quad (45)$$

The term $-\Lambda \mathbf{u}$ has the form of a Darcy or Rayleigh drag, showing that the sublayer behaves like a porous medium on the timescale set by the strain flow. The μ -choke together with the sublayer's flatness and thinness act to keep the flow nearly horizontal, compelling it to push past, and slightly deflect, the magnetic field lines spanning the sublayer at angles steep by comparison with sublayer aspect ratios. In this Darcy regime we have

$$u_r = -\Lambda u_\phi, \quad (46)$$

$$\frac{\partial u_\phi}{\partial z} = -\alpha_\mu \frac{\partial \mu}{\partial r} + \Lambda \frac{\partial u_r}{\partial z} \quad (47)$$

in place of (15) and (16). Together with (7) and (11), equations (46) and (47) describe the sublayer dynamics to an order of accuracy that includes the first corrections to perfect flatness.

We now use scaling arguments, paralleling those in §5, to verify that the corrections can indeed be taken as small and the sublayer treated as flat. As before, we expect that each term in (47) is proportional to r and that

$$\mu = a_\mu + \frac{1}{2} b_\mu r^2 \quad (48)$$

to good approximation close to the pole, where r is again dimensionless and where a_μ and b_μ are

dimensionless functions of z alone. The matching to the helium settling layer beneath implies that $da_\mu/dz \sim 1$, and that $a_\mu \sim \delta_\chi/\delta$ if we take the constant value of μ aloft to be zero. The condition for validity of flat sublayer solutions is $r^2 \ll r_\mu^2$, say, where r_μ denotes a typical magnitude of $|a_\mu/b_\mu|^{1/2}$.

Within the sublayer, the pattern of dimensionless scalings (21)–(26) is replaced by

$$u_z \sim \delta_\chi/\delta \quad (49)$$

$$u_r \sim r \quad (50)$$

$$u_\phi \sim r\Lambda^{-1} \quad (51)$$

$$B'_z \sim \Lambda^{1/2} (\delta_\chi/\delta)^2 \quad (52)$$

$$B'_r \sim r\Lambda^{1/2} \delta_\chi/\delta \quad (53)$$

$$B'_\phi \sim r\Lambda^{-1/2} \delta_\chi/\delta \quad (54)$$

for all $r \lesssim r_\mu$, on the provisional assumption that the near-pole behavior of the fields correctly indicates orders of magnitude out as far as $r \sim r_\mu$. These dimensionless order-of-magnitude relations follow from the matching to the confinement layer and from $\nabla \cdot \mathbf{B}' = \nabla \cdot \mathbf{u} = 0$ together with (44) and (46), where $\partial/\partial z \sim \delta/\delta_\chi \gg 1$. Again, further detail is given in Appendix A.

The horizontal velocity components in (50)–(51) inherit their magnitudes directly from those in the overlying confinement layer. By contrast, the horizontal \mathbf{B}' components in (53)–(54) contain the small factor δ_χ/δ , arising from a balance between the two terms on the right of (44). It is noteworthy that the relatively strong vertical shear in the horizontal velocity components explains how in the limit $\delta_\chi \rightarrow 0$, preserving (41), the sublayer regime goes over into the slip regime analyzed in WM07. The slip regime has infinite shear at the top of the helium settling layer, with discontinuities in both horizontal velocity components.

We can now estimate r_μ and hence the flatness of the sublayer, by assuming provisionally that (48) remains valid as a guide to orders of magnitude out to $r \sim r_\mu$. Then $\partial\mu/\partial r \sim b_\mu r$ at all $r \lesssim r_\mu$, so that the α_μ term in (47) has magnitude $\sim \alpha_\mu b_\mu r$. From (49)–(54) we see that the other terms in (47) have magnitudes $\sim r(\delta/\delta_\chi)\Lambda^{-1}$ (the term in u_ϕ) and $\sim r(\delta/\delta_\chi)\Lambda$ (the term in u_r). The typical magnitude of $\alpha_\mu b_\mu$ can therefore be taken to be $(\delta/\delta_\chi) \max(\Lambda, \Lambda^{-1})$. Correspondingly, since

$a_\mu \sim \delta_\chi/\delta$, we may define r_μ^2 , the typical magnitude of a_μ/b_μ , to be $\alpha_\mu(\delta_\chi/\delta)^2 \min(\Lambda, \Lambda^{-1}) = \alpha_\mu(\chi/\eta) \min(\Lambda, \Lambda^{-1})$. Comparing this with (27) and recalling that $\alpha_\mu = N_\mu^2 \delta^2 / 2\Omega_i \eta$ we see that

$$r_\mu^2 = \frac{N_\mu^2}{N_T^2} \frac{\kappa \chi}{\eta^2} r_T^2 \gg r_T^2, \quad (55)$$

since $\kappa \chi / \eta^2 \approx 0.75 \times 10^3$. So, although the foregoing scale analysis cannot be taken literally all the way out to $r \sim r_\mu$, it clearly tells us that the sublayer is very flat indeed, even at $r \sim r_T$ where the tilting of thermal stratification surfaces is significant within the confinement layer. In summary, our flatness assumptions hold even more strongly for the sublayer than for the confinement layer.

It is worth going beyond scale analysis to say more about the vertical structure of the sublayer, especially in its lower extremity or “subtail”, wherein we expect the MMC to decay exponentially with depth as the μ -choke takes hold. Within this subtail, the helium settling layer suffers only small perturbations to its otherwise uniform compositional stratification $\partial\mu/\partial z = -1$. We denote the perturbation to μ by μ' . In the steady state, equation (11) may then be approximated as

$$-u_z = \frac{\chi}{\eta} \frac{\partial^2 \mu'}{\partial z^2}, \quad (56)$$

which can be combined with (7), (46), and (47) to yield a single equation for the perturbation μ' ,

$$\alpha_\mu(\eta/\chi) \nabla_H^2 \mu' = (\Lambda + \Lambda^{-1}) \frac{\partial^4 \mu'}{\partial z^4}, \quad (57)$$

where $\nabla_H^2 = r^{-1} \partial(r \partial/\partial r)/\partial r = \nabla^2 - \partial^2/\partial z^2$. It is now clear that the leading-order scale analysis given above applies only to the main part of the sublayer and not to the subtail. Equation (57) tells us that the vertical scale, δ_ℓ say, for the subtail must depend on the horizontal scale in a manner reminiscent of the heuristic boundary-layer analysis given in GM98.

For instance if we assume that the actual horizontal scale is the scale r_T set by the confinement layer, so that $\alpha_\mu \nabla_H^2 \mu' \sim \alpha_\mu r_T^{-2}$, then a straightforward scale analysis of (57) shows that, in terms of the definitions (27) and (55),

$$\delta_\ell \sim \left(\frac{r_T}{r_\mu} \right)^{\frac{1}{2}} \delta_\chi, \quad (58)$$

which is smaller than δ_χ . Even at this scale, however, viscosity remains negligible provided that the Darcy friction from the field lines dominates the fluid friction from molecular viscosity. That is, viscosity remains negligible provided that

$$\Lambda \gg \text{Ek} \nabla^2 \sim \text{Ek} (\delta/\delta_\ell)^2, \quad (59)$$

$$\text{equivalently} \quad \delta_\ell^2 \gg \delta_{\text{Ek}}^2 / \Lambda, \quad (60)$$

which for realistic solar parameters is easily satisfied because $\text{Ek} \sim 0.4 \times 10^{-8}$. A more detailed analysis (Wood 2010) verifies all these properties of the subtail. The exponentially weak flow within the subtail is invisible in Fig. 2, and barely visible in Fig. 3.

8. THE NUMERICAL SOLUTIONS

Unfortunately it is not possible to solve the complete set of equations (6)–(11) analytically. To go beyond the self-similar, perfectly flat solutions described in §6 we must compute solutions numerically. To this end a numerical code has been written to solve the axisymmetric version of (6)–(11) in a cylinder of radius r_d . The scheme on which the code is based is summarized in Appendix B. Computing limitations preclude a perfect match to the real Sun’s parameter values. They also require a slight modification to (6)–(11), explained in Appendix B, in which artificial horizontal diffusivities ν_H, χ_H are introduced in order to maintain numerical stability. However, from the foregoing scale analyses we may identify the conditions most essential to reaching a qualitatively similar parameter regime — that is, qualitatively similar to a regime with a perfect parameter match to the real Sun. These essential conditions are:

1. The Rossby number Ro should be small in comparison with unity, so that the steady state is close to magnetostrophic.
2. The thermal diffusivity κ should be large in comparison with the magnetic diffusivity η , so that the confinement-layer flow only weakly perturbs the background thermal stratification.
3. The confinement layer and helium sublayer should both be reasonably flat, at least within the numerical domain $r \leq r_d$. With (55) in mind, we also take $r_\mu > r_T$, where $r_T > r_d > 1$.

4. The helium diffusivity χ should be small in comparison with the magnetic diffusivity η , so that the helium sublayer is thinner than, and therefore distinct from, the magnetic confinement layer.
5. The viscosity ν should be small enough that an Ekman layer does not form at the top of the helium settling layer, and the flow is everywhere inviscid, even in the helium sublayer. With small Ro this condition is easily satisfied in the numerical model as well as in the real Sun, by (40).

Leaving ν_H and χ_H aside for the moment (see Appendix B) we can characterize the system by seven dimensionless parameters, including the Elsasser number Λ , which enters through the boundary conditions. Table 1 presents the other six dimensionless parameters, beginning with nominal solar values alongside the values used in the numerical solution presented in this paper (Figs. 2, 5, and 6). The last column echoes aspects of the qualitative parameter conditions just stated. The solar values assume $U = 10^{-5} \text{ cm s}^{-1}$.

In the solutions, the value of Λ is set indirectly via the boundary condition for B_r . For the case shown in Figs. 2, 5, and 6 this boundary condition was $B_r/r = 1$ on the bottom of the domain, and from Fig. 6 we see that $\Lambda = B_{iz}^2|_{z=0} \approx 3.5$. The nominal range of Λ for which solutions are nearly flat within dimensionless radius r is determined by (27) with $r_T > r$. With the parameter values in the second-last column of Table 1, $r_T > r$ is

Table 1: Parameter values and conditions; see text.

Dim'less parameter	Nominal solar value	Value for num. sol'n	Condition
Ro	5×10^{-8}	10^{-2}	$\ll 1$
κ/η	3×10^4	10^2	$\gg 1$
$\alpha_T(\eta/\kappa)$	2×10^7	50	$> \max(\Lambda, \Lambda^{-1})^a$
$(r_\mu/r_T)^2$	3×10^2	2	> 1
χ/η	2×10^{-2}	2×10^{-2}	$\ll 1$
ν/χ	3	1	$\ll 1/\text{Ro}$

^aThis condition follows from $r_T > 1$, with $r_T^2 = \alpha_T(\eta/\kappa) \min(\Lambda, \Lambda^{-1})$ as shown just above (27).

equivalent to

$$\max(\Lambda, \Lambda^{-1}) < 50/r^2. \quad (61)$$

Since $\Lambda \approx 3.5$, (61) is violated near the edge of the domain, $r = r_d = 5$. Nevertheless, as seen for instance in Fig. 2, the solution remains fairly close to being flat.

As noted in §4, the thermal boundary conditions cannot be fully specified without fitting the polar confinement layer into the complete picture of the perturbed global-scale heat flow. For simplicity, we have imposed that T is constant at the top of the domain, which is consistent with the imposed uniform downwelling aloft along with small departures from flatness. However, from equation (16) we see that this boundary condition, in the case of large but finite flatness, implies vanishing vertical shear in the field-free region aloft. Matching the confinement layer onto the observed negative vertical shear in the bulk of the tachocline is beyond the scope of this study, for reasons mentioned in §4.

The vertical profiles of T , μ and B_ϕ at the periphery of the computational domain were initially taken from a self-similar solution. The resulting steady-state meridional flow, and the Coriolis torque it exerts on each field line, cannot be precisely known in advance. So the steady state found, with this choice of B_ϕ , will generally include a non-trivial profile of Alfvénic torque exerted at the bottom of the computational domain. This is inconsistent with the picture presented in Fig. 1, in which \mathbf{B}_i is dipolar and no Alfvénic torque is exerted on the top of the helium settling layer.

Any such torque, were it to persist in the real Sun, would lead to a buildup of differential rotation between neighboring “Ferraro surfaces”, i.e., poloidal magnetic flux surfaces, throughout an “apple-core” region surrounding the rotation axis in the interior and extending between the two polar confinement layers. But any such differential rotation would be limited by dynamical instabilities, whether MRI, Tayler, or barotropic hydrodynamic shear instabilities, giving rise to quasi-frictional angular momentum coupling between the neighboring Ferraro surfaces. Through such coupling the interior can bring the torque between the apple core and the two confinement layers down to small values, thus reshaping the confine-

ment-layer flow, and with it the peripheral torque profiles between the confinement layers and the extra-polar overshoot layer.

With our axisymmetric local model of the confinement layers we cannot directly model the interaction just described, nor the other interactions between each confinement layer and its surroundings. Instead, we make iterative adjustments to the peripheral B_ϕ profile, aiming to make the Alfvénic torque at the bottom of the computational domain vanish in the steady state.

Figure 5 shows plots of the steady-state streamlines and magnetic field lines from the numerical solution whose parameter values are listed in Table 1, and whose meridional cross-section was presented in Fig. 2. Figure 6 shows the vertical profiles of u_z , u_ϕ/r , B_z and B_ϕ/r on the rotation axis, from the same numerical solution.

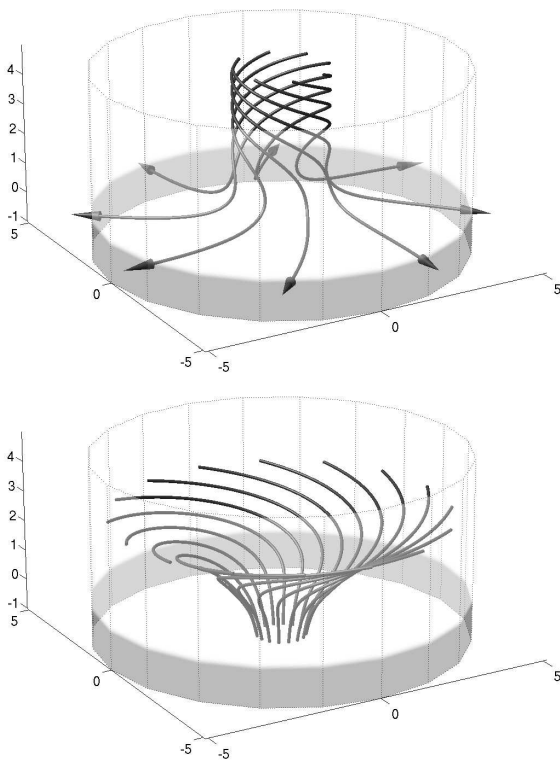


Fig. 5.— A numerical solution of the confinement-layer equations with $r_T^2 \approx 14$ and Elsasser number $\Lambda \approx 3.5$. Other parameter values are given in the second-last column of Table 1. From the same solution as shown in Fig. 2.

9. UPPER-DOMAIN “SLIPPERINESS”

On the rotation axis, where the profiles in Fig. 6 were taken, the stratification surfaces are flat for any finite r_T , and the structure is therefore self-similar. If the numerical solution were in perfect magnetostrophic balance then we could use its $u_z(z)$ profile to calculate the other field components on the axis by the procedure for constructing self-similar solutions described in §6. But the numerical solutions are not in perfect balance, especially toward the upper part of the domain, where the Lorentz and Coriolis forces become small and the artificial viscous forces relatively more significant, along with numerical truncation errors and any other small effects. In particular, the numerical $u_z(z)$ will not conform to the decay law (37) as z increases. So the self-similar solution obtained by this process cannot perfectly match the numerical solution, even on the axis. Indeed, such a self-similar solution will often exhibit wild deviations from the numerical solution toward the upper part of the domain. There, the delicate balance of terms gives the dynamics a certain “slipperiness”, as already evidenced by the upper-domain sensitivity to values of the decay constant γ in (37).

To enable a meaningful comparison between the numerical and analytical solutions, we are therefore compelled to make small adjustments to $u_z(z)$ in the upper domain, to make it conform to (37), before using it to compute a self-similar solution. In the case shown here the required adjustment to $u_z(z)$ is very small indeed. The solid u_z curves on the left of Figs. 3 and 6 are practically indistinguishable.

10. CONCLUSIONS AND FUTURE DIRECTIONS

We cannot yet claim to have a complete tachocline theory, because the confinement layer and helium sublayer form only two pieces of a complicated jigsaw puzzle. Other pieces include the way in which the confinement layer matches upward to the negative shear in the bulk of the tachocline, and the way in which the baroclinic temperature anomalies induced by the tachocline’s MMC fit into the perturbed global-scale heat flow. In particular, without putting the whole jigsaw together we cannot quantitatively predict the thickness of the tachocline. That remains a challenge for the

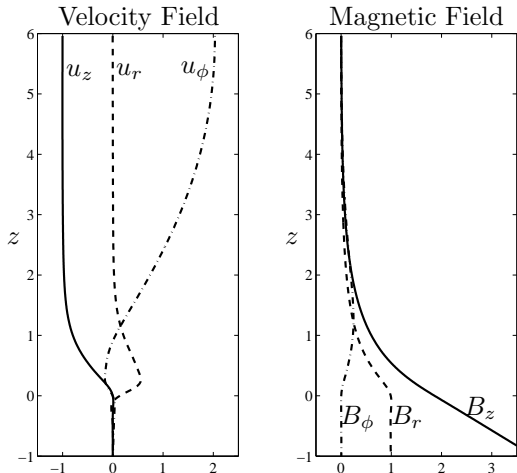


Fig. 6.— Vertical profiles from a numerical solution of the confinement-layer equations with $r_T^2 \approx 14$ and Elsasser number $\Lambda \approx 3.5$. Other parameter values are given in the second-last column of Table 1. From the same solution as shown in Fig. 2.

future. However, we have obtained the first fully consistent picture of polar field confinement and how it could work in today’s Sun.

We can also use the resulting insights alongside our well-established understanding of hydrodynamic spreading or burrowing, mentioned in §1, to say something useful about the early Sun and the lithium-burning problem.

The downwelling MMC in the polar tachocline that makes field confinement possible can be regarded as due to a gyroscopically-pumped MMC trying, as it were, to burrow down but held in check by its encounter with the interior field and helium settling layer.

Because the early Sun rotated much faster than today, the burrowing tendency would have been stronger than today, tending to push the bottom of the tachocline downward. Ventilation to greater depths during the first gigayear or so of the Sun’s main-sequence evolution might prove to be the long-sought explanation for the Sun’s observed lithium and beryllium abundances. This reopens the possibility conjectured in GM98 that there might have been a ventilated “polar pit” or “cauldron” in which lithium was burnt.

In the absence of a helium settling layer, as in the earliest part of the Sun’s main-sequence evo-

lution (because of Hayashi-phase chemical homogenization) we have $N_\mu \approx 0$ but can still construct self-similar solutions to the confinement-layer equations in the same way as in §6. The confinement-layer dynamics works in the same way as before (details omitted). The interior field \mathbf{B}_i is therefore enough by itself to hold the burrowing in check, as originally proposed in GM98. In these zero- N_μ solutions, the helium sublayer is absent and the MMCs penetrate a bit further into the radiative envelope, on vertical scales δ rather than the scales δ_χ and δ_ℓ discussed in §7.

However, this deeper penetration is insufficient by itself to account for the formation of a lithium-burning cauldron because δ , though greater than δ_χ and δ_ℓ , is still only a fraction of a megameter. There is also the overall flatness of the stratification surfaces, a robust feature even on the global scale, as argued for instance in §8.5 of McIntyre (2007). What is probably more important is the way in which the confinement layer fits into the global picture. It is arguable that the entire polar downwelling region is depressed relative to its surroundings, forming a wider cauldron, too shallow to burn lithium in today’s Sun but possibly deep enough in the early Sun.

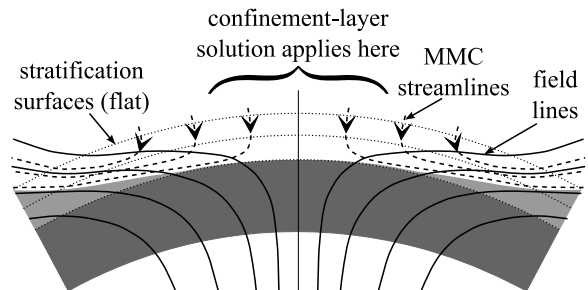


Fig. 7.— Sketch of the magnetic confinement layer and its immediate surroundings at the bottom of the high-latitude tachocline. Close to the pole the interior magnetic field (solid lines) is confined by the downwelling MMC (dashed streamlines). The vertical scale has been greatly exaggerated.

Here we need to distinguish the shape of the ventilated region from that of the stratification surfaces, which latter must remain relatively flat, meaning close to the horizontal or equivalently, in a global picture, close to the isobaric surfaces. Figure 7 sketches the way in which the confinement layer might fit into its surroundings near the

bottom of the polar tachocline. The stratification surfaces are shown dotted. At the periphery of the polar downwelling region, the field lines (solid) emerge from the confinement layer on their way to lower latitudes. They will tend to splay out and slant upward as they exit the downwelling region. The MMC will similarly slant upward, flowing approximately along the field lines (dashed streamlines). This is because the splaying-out increases the magnetic Reynolds number beyond the order-unity values characteristic of the confinement layer. Further out, the field lines must continue to rise through the tachocline until they encounter the convection zone's overshoot layer, where they are held horizontal by turbulent magnetic flux pumping. On the way we must expect turbulent eddy fluxes to become increasingly important, decoupling the MMC's upwelling streamlines from the time-averaged field lines and leaving the upwelling free to spread over a wide range of latitudes, constrained only by mass conservation and global-scale heat flow.

Such a picture applies equally well to today's Sun and to the early Sun, the main difference being that the ventilated polar region (unshaded in Fig. 7) is likely to have been pushed deeper in the early Sun with its much faster rotation, stronger burrowing tendency, and global-scale $|\mathbf{B}_i|$ values only modestly larger. The ventilated polar region could well have been deeper by many tens of megameters, as required to burn lithium.

Within the peripheral lightly-shaded region, into which the MMC does not penetrate, we suggest that ventilation is weak or nonexistent and that shear will be limited by the Ferraro constraint. The darker shading represents the top part of today's helium settling layer.

As the lightly-shaded region expands upward and outward beyond the immediate surroundings sketched in Fig. 7, through the tachocline toward the overshoot layer, we may surmise that Tayler or magnetorotational small-scale MHD instabilities will kick in (e.g., Spruit 2002; Gilman & Cally 2007; Parfrey & Menou 2007, & refs.), breaking the Ferraro constraint and blurring the distinction between the shaded and unshaded regions as turbulent eddy fluxes increase. So a larger-scale picture of the cauldron would show its upward-sloping lower boundary becoming increasingly porous and indistinct at greater colatitudes.

The global tachocline model that would be needed to test, and to begin to quantify, the foregoing speculations would have to describe

1. the precise way in which turbulent stresses in the convection zone and tachocline gyroscopically pump the polar downwelling responsible for confining \mathbf{B}_i ;
2. the global-scale distribution of temperature and heat flow that fits in with these MMCs;
3. the turbulent magnetic flux pumping by convective overshoot that we assume confines \mathbf{B}_i in extra-polar latitudes;
4. the extent to which the winding-up of the time-averaged toroidal field in extra-polar latitudes (Fig. 1) is limited by turbulent eddy fluxes;
5. the reaction of the overlying turbulent layers to all of the above, especially the deficit in the convection zone's differential rotation governing the torques exerted from above, whether via gyroscopically-pumped MMCs or via turbulent stresses in the bulk of the tachocline, or via both.

Progress on these formidable problems will of course depend on finding suitable ways to model the turbulent processes.

Finally, we note that transport by burrowing MMCs is not the only possible explanation for the Sun's observed lithium abundance. For instance early main-sequence mass loss, perhaps followed by lithium production by flares, might have had a role (e.g., Swenson & Faulkner 1992, L. A. Willson, personal communication).

We thank N. H. Brummell, P. Garaud, D. O. Gough, D. Jault, C. A. Jones, M. R. E. Proctor, T. M. Rogers, S. M. Tobias, N. O. Weiss, and L. A. Willson for helpful and stimulating discussions. TSW was supported by a UK Science and Technology Facilities Council Research Studentship.

A. HELIUM SUBLAYER SCALINGS

For perturbations \mathbf{B}' to a background magnetic field \mathbf{B}_i , the Lorentz force may be written as

$$\mathbf{F} = (\nabla \times (\mathbf{B}_i + \mathbf{B}')) \times (\mathbf{B}_i + \mathbf{B}') = -\nabla \left(\frac{1}{2} |\mathbf{B}_i|^2 + \mathbf{B}_i \cdot \mathbf{B}' + \frac{1}{2} |\mathbf{B}'|^2 \right) + (\mathbf{B}_i + \mathbf{B}') \cdot \nabla (\mathbf{B}_i + \mathbf{B}') \quad (\text{A1})$$

If, as here, the background field \mathbf{B}_i is curl-free, then all the terms quadratic in \mathbf{B}_i vanish and we have

$$\mathbf{F} = -\nabla (\mathbf{B}_i \cdot \mathbf{B}' + \frac{1}{2} |\mathbf{B}'|^2) + \mathbf{B}' \cdot \nabla \mathbf{B}_i + (\mathbf{B}_i + \mathbf{B}') \cdot \nabla \mathbf{B}'. \quad (\text{A2})$$

If \mathbf{B}_i and \mathbf{B}' are axisymmetric, and have the scalings given by (52)–(54), with $\partial/\partial z \sim \delta/\delta_\chi \gg 1$, then all components of $\mathbf{B}' \cdot \nabla \mathbf{B}'$ are smaller than the corresponding components of $\mathbf{B}_i \cdot \nabla \mathbf{B}'$ by factors $(\delta_\chi/\delta)^2$, with one exception. The r component of $\mathbf{B}' \cdot \nabla \mathbf{B}'$ includes a term $B_\phi'^2/r$, the divergence of the hoop stress. Relative to the r component of $\mathbf{B}_i \cdot \nabla \mathbf{B}'$ this is of order $(\delta_\chi/\delta)^2/\Lambda^2$. However, the hoop-stress term is smaller than the r component of the Coriolis force by a factor $(\delta_\chi/\delta)^2$, even for small Λ , because of (51). We also find that, because $B_{i\phi} = 0$, the poloidal components of $\nabla (\mathbf{B}_i \cdot \mathbf{B}')$ exceed in magnitude those of $\nabla (\frac{1}{2} |\mathbf{B}'|^2)$ by a factor $(\delta/\delta_\chi)^2$. Their azimuthal components are both zero since we consider only axisymmetric fields here. We may therefore neglect all terms quadratic in \mathbf{B}' , in the asymptotic regime (41), so that (14) becomes

$$\mathbf{e}_z \times \mathbf{u} = -\nabla p + \alpha_T T \mathbf{e}_z - \alpha_\mu \mu \mathbf{e}_z - \nabla (\mathbf{B}_i \cdot \mathbf{B}') + \mathbf{B}' \cdot \nabla \mathbf{B}_i + \mathbf{B}_i \cdot \nabla \mathbf{B}'. \quad (\text{A3})$$

The flow through the sublayer produces only a small perturbation to the otherwise uniform thermal stratification. From (10) and (11) we see that, within the sublayer, variations in T are smaller than variations in μ by a factor $\chi/\kappa \ll 1$. The thermal stratification in the sublayer may therefore be treated as horizontally uniform, allowing the thermal buoyancy term $\alpha_T T \mathbf{e}_z$ in (A3) to be incorporated into the pressure field along with the $-\nabla (\mathbf{B}_i \cdot \mathbf{B}')$ term.

The perturbed steady-state induction equation is

$$0 = (\mathbf{B}_i + \mathbf{B}') \cdot \nabla \mathbf{u} - \mathbf{u} \cdot \nabla (\mathbf{B}_i + \mathbf{B}') + \nabla^2 \mathbf{B}', \quad (\text{A4})$$

again on the assumption that \mathbf{B}_i is curl-free. It is readily verified from the scalings (49)–(54) and $\partial/\partial z \sim \delta/\delta_\chi \gg 1$ that each component of $\mathbf{u} \cdot \nabla \mathbf{B}'$ is of the same order as the corresponding component of $\mathbf{B}' \cdot \nabla \mathbf{u}$, but smaller than $\mathbf{B}_i \cdot \nabla \mathbf{u}$ by a factor $(\delta_\chi/\delta)^2$. Furthermore, provided that the horizontal scales r_T and r_μ are both $\gg 1$ we may also make the boundary-layer approximation, $\nabla^2 \approx \partial^2/\partial z^2$. Thus, in the asymptotic regime (41), we may simplify (A4) to

$$0 = \mathbf{B}_i \cdot \nabla \mathbf{u} - \mathbf{u} \cdot \nabla \mathbf{B}_i + \frac{\partial^2}{\partial z^2} \mathbf{B}'. \quad (\text{A5})$$

If the field \mathbf{B}_i were uniform, and directed along the axis of rotation, then (A3) and (A5) would reduce immediately to (42) and (43). Since \mathbf{B}_i is axisymmetric and smooth, this reduction still holds as a first approximation within some neighborhood of the axis. It is sufficient to show that this neighborhood includes the entire sublayer within a radius $r \sim r_\mu$. We first note that, since $\nabla \cdot \mathbf{B}_i = 0$, we have $B_{ir}/r = -\frac{1}{2} \partial B_{iz}/\partial z$, by analogy with (35). In the sublayer we have $\partial B_{iz}/\partial z \sim B_{iz}$ (dimensionally, $\partial B_{iz}/\partial z \sim B_{iz}/\delta$) as a consequence of the matching to the confinement layer, as can be seen, for instance, from the solid curve in the right-hand panel of Fig. 3. Now applying the scalings (49)–(54) we find that, in (A3), each component of $\mathbf{B}' \cdot \nabla \mathbf{B}_i$ is smaller than the corresponding component of $\mathbf{B}_i \cdot \nabla \mathbf{B}'$ by a factor δ_χ/δ , and that, in (A5), each component of $\mathbf{u} \cdot \nabla \mathbf{B}_i$ is smaller than the corresponding component of $\mathbf{B}_i \cdot \nabla \mathbf{u}$ by the same factor δ_χ/δ . Moreover, even at colatitudes $r \sim r_\mu$ the contributions $B_{iz} \partial \mathbf{B}'/\partial z$ and $B_{iz} \partial \mathbf{u}/\partial z$ dominate all other contributions to $\mathbf{B}_i \cdot \nabla \mathbf{B}'$ and $\mathbf{B}_i \cdot \nabla \mathbf{u}$ by factors of at least δ/δ_χ . So (A3) and (A5) do indeed reduce to (42) and (43).

Within the region $r \leq r_\mu$, tilting of the compositional isopleths produces variations in the altitude of the sublayer of no more than $O(\delta_\chi/\delta)$, so that B_{iz} may be assumed constant within the sublayer, as assumed

in the derivation of (46) and (47). Finally, we note that the foregoing picture applies not only to steady states but also to time-dependent states with any timescale, such as δ/U , that is long in comparison with the timescale δ_χ^2/η for magnetic diffusion across the sublayer. On any such timescale the sublayer therefore behaves like a porous medium.

B. THE NUMERICAL SCHEME

We wish to solve a suitable version of equations (6)–(11) in axisymmetric cylindrical polar coordinates. We introduce streamfunctions Ψ and A , i.e., azimuthal vector-potential components, for the poloidal velocity and magnetic fields, such that

$$u_z = \frac{1}{r} \frac{\partial(r\Psi)}{\partial r} \quad \text{and} \quad u_r = -\frac{\partial\Psi}{\partial z}, \quad (\text{B1})$$

$$B_z = \frac{1}{r} \frac{\partial(rA)}{\partial r} \quad \text{and} \quad B_r = -\frac{\partial A}{\partial z}, \quad (\text{B2})$$

guaranteeing that the fields are divergence-free. In the fluid-dynamical literature $r\Psi$ is sometimes called the Stokes streamfunction. The azimuthal vorticity ω_ϕ and electric current J_ϕ are related to Ψ and A by

$$\omega_\phi = -(\nabla^2 - r^{-2})\Psi \quad (\text{B3})$$

and

$$J_\phi = -(\nabla^2 - r^{-2})A. \quad (\text{B4})$$

For numerical reasons described below, we introduce anisotropic viscosity and helium diffusivity with dimensionless horizontal components ν_H and χ_H . So equations (6)–(11) are replaced by

$$\text{Ro} \frac{1}{r} \frac{\text{D}(ru_\phi)}{\text{D}t} - \frac{\partial\Psi}{\partial z} = \frac{1}{r} \mathbf{B} \cdot \nabla(rB_\phi) + \text{Ek} \left[\frac{\partial^2}{\partial z^2} + \nu_H \left(\nabla_H^2 - \frac{1}{r^2} \right) \right] u_\phi \quad (\text{B5})$$

$$\begin{aligned} \text{Ro} \left[r \frac{\text{D}(\omega_\phi/r)}{\text{D}t} + \frac{\partial(ru_\phi, u_\phi/r)}{\partial(z, r)} \right] - \frac{\partial u_\phi}{\partial z} = & -\alpha_T \frac{\partial T}{\partial r} + \alpha_\mu \frac{\partial \mu}{\partial r} + r \mathbf{B} \cdot \nabla(J_\phi/r) + \frac{\partial(rB_\phi, B_\phi/r)}{\partial(z, r)} \\ & + \text{Ek} \left[\frac{\partial^2}{\partial z^2} + \nu_H \left(\nabla_H^2 - \frac{1}{r^2} \right) \right] \omega_\phi \end{aligned} \quad (\text{B6})$$

$$r \frac{\text{D}(B_\phi/r)}{\text{D}t} = r \mathbf{B} \cdot \nabla(u_\phi/r) + \left(\nabla^2 - \frac{1}{r^2} \right) B_\phi \quad (\text{B7})$$

$$\frac{1}{r} \frac{\text{D}(rA)}{\text{D}t} = \left(\nabla^2 - \frac{1}{r^2} \right) A \quad (\text{B8})$$

$$\frac{\text{D}T}{\text{D}t} = \frac{\kappa}{\eta} \nabla^2 T \quad (\text{B9})$$

$$\frac{\text{D}\mu}{\text{D}t} = \frac{\chi}{\eta} \left[\frac{\partial^2}{\partial z^2} + \chi_H \nabla_H^2 \right] \mu \quad (\text{B10})$$

Because of the axisymmetric cylindrical geometry, the lack of spatial periodicity, and the wide range of spatial scales inherent in the polar confinement-layer problem, a spectral or pseudospectral code would be unsuited to the task of solving these equations. Instead, a simple finite-difference code has been written in cylindrical polar coordinates, with an Eulerian grid regularly spaced in r and z at intervals Δr and Δz . The outer boundary of the computational domain is at $r = r_d$. The inner boundary is at $r = 2\Delta r$, i.e., two grid intervals from the coordinate singularity at the rotation axis. Because of the directionality of operators like $\mathbf{u} \cdot \nabla$ and $\mathbf{B} \cdot \nabla$, the spatial derivatives are calculated using two-point, one-sided (first-order) finite differences whose directions are chosen to ensure numerical stability at the grid scale. For reasons of symmetry and good behavior near the coordinate singularity, the finite differencing is done by locally approximating the

fields Ψ/r , u_ϕ/r , ω_ϕ/r , A/r , B_ϕ/r , T , and μ as functions that are linear in z and in r^2 over a single grid interval. This ensures that the error is $O(\Delta r)$ even for small r . Field values for $r < 2\Delta r$ are obtained by extrapolation from $r = 3\Delta r$ and $r = 2\Delta r$, again assuming linear functional dependence on r^2 .

With the parameter values given in Table 1, the dimensionless helium-sublayer and Ekman-layer thicknesses are $\delta_\chi/\delta = (\chi/\eta)^{1/2} \approx 0.14$ and $\delta_{\text{Ek}}/\delta = \text{Ek}^{1/2} \approx 0.01$ respectively. We have chosen a vertical grid interval $\Delta z = 0.01$, dimensionally 0.01δ , which is small enough to resolve the helium sublayer accurately. This Δz is too large to resolve any Ekman layers. However, Ekman layers are prevented from becoming significant by careful choice of the code representing the boundary conditions. By allowing slip velocities and making viscous stresses negligible at the boundaries, we have been able to keep Ekman-layer formation so weak as to play no significant role in the dynamics. Uniform rotation is imposed at the bottom of the domain via the $\mathbf{B} \cdot \nabla$ term in the azimuthal component of the induction equation (B7), exploiting the Alfvénic torques in the system.

An explicit Eulerian timestepping scheme is used to evolve the system. The timestep Δt must be small enough to resolve thermal diffusion at the grid scale (which is the fastest process at this scale and therefore determines the Courant–Friedrichs–Lewy condition). So from Table 1, $\Delta t \lesssim (\eta/\kappa)(\Delta z)^2 = 10^{-2} \times (0.01)^2 = 10^{-6}$, dimensionally $10^{-6}\delta/U$ or $10^{-4}(2\Omega_i)^{-1}$. The system typically takes several domain-scale magnetic diffusion times to reach a steady state, and multiple iterations of the peripheral $B_\phi(z)$ profile are required to achieve a steady state with vanishing $B_\phi(r)$ at the bottom. To make the computation feasible, in a domain wide enough to accommodate noticeable tilting effects, we have used $r_d = 5$, dimensionally 5δ , and a horizontal grid interval $\Delta r = 0.1$, dimensionally 0.1δ , larger than the vertical grid interval Δz by a factor of 10. For numerical stability, we found it necessary to increase the horizontal viscosity and helium diffusivity each by a factor of 10, i.e., $\nu_H = \chi_H = 10$. We have verified, in smaller computational domains, that the coarser horizontal resolution and the anisotropic diffusion do not qualitatively affect the steady state of the system. The increased horizontal viscosity introduces stronger angular momentum coupling between neighboring Ferraro surfaces, and typically brings the system’s steady state closer to uniform rotation. In this sense the artificial viscosity acts rather like the hypothesized shear-induced turbulence mentioned in §8.

At each timestep, the azimuthal vorticity ω_ϕ is updated and the streamfunction Ψ then computed from (B3) by inverting the operator $\nabla^2 - r^{-2}$, approximated using centered differences. The inversion is performed iteratively, using a successive-overrelaxation method described in Press et al. (1986). During the early evolution, when the dynamics is dominated by timescales not much longer than the timestep Δt , many such iterations are required, at each timestep, to achieve convergence. At later times the same degree of convergence can be achieved with far fewer iterations. Since we are interested only in the ultimate steady state, we can tolerate a larger error in the inversion during the system’s transient evolution. Further details of the numerical code are spelt out in Wood (2010).

As anticipated from scaling arguments, the steady state is found to be close to magnetostrophic balance. It might be thought that imposing magnetostrophic balance throughout the evolution, as first suggested by Taylor (1963), would filter out all the fast oscillations, including inertial or epicyclic oscillations, and thereby allow larger timesteps to be used. However, the imposition of magnetostrophic balance leads to pathological behavior at small scales (Walker et al. 1998). Far from eliminating or slowing the fast oscillations, the imposition of balance exacerbates the problem, for reasons explained in Appendix C.

C. MAGNETOSTROPHIC BALANCE AND NUMERICAL ILL-CONDITIONEDNESS

Because the confinement-layer problem involves only steady or nearly-steady flow, it is natural to try to save computational resources by filtering out the fast oscillations (e.g., Taylor 1963). These include Alfvén waves, gravity waves, inertia/Coriolis/epicyclic waves and the various hybrid types. Such filtering is familiar, and often effective, in many other problems involving stiff differential equations. A well known example is that of fluid flow in non-MHD fluid systems with strong rotation and stable stratification. The standard “quasi-geostrophic equations” result from small-Ro approximations that filter out inertia and gravity waves,

as well as sound waves, allowing relatively large time steps.

Such filtering turns out, however, to be ineffective in the confinement-layer problem. Indeed — at first sight paradoxically — the imposition of magnetostrophic balance leads to pathological behavior in the following sense. Far from eliminating fast oscillations, it introduces spurious modes of oscillation that are even faster, as shown by Walker et al. (1998) in the context of the terrestrial dynamo problem. Following Walker et al., we show how the pathology can be understood through an idealized analysis of the fast oscillations, first in the unfiltered and then in the filtered equations.

The reason for the pathology is the interplay between the Coriolis and Lorentz forces. Stratification N^2 is relatively unimportant, as will be shown shortly. We therefore start with the linear theory of MC (magneto–Coriolis) waves, i.e., small plane-wave disturbances to an unstratified, incompressible fluid with uniform rotation $\boldsymbol{\Omega}$ and a uniform magnetic field \mathbf{B} . Neglecting viscosity and magnetic diffusivity, we find the well-known dispersion relation

$$\omega^2 - (\mathbf{B} \cdot \mathbf{k})^2 = \pm 2\boldsymbol{\Omega} \cdot \mathbf{k} \omega / |\mathbf{k}|, \quad (\text{C1})$$

where ω is the frequency and \mathbf{k} is the wavevector, both dimensional here. If we take the limit of rapid rotation, $|\boldsymbol{\Omega}| \rightarrow \infty$, then for most choices of \mathbf{k} the four roots of this dispersion relation are asymptotically

$$\omega \sim \pm \frac{2\boldsymbol{\Omega} \cdot \mathbf{k}}{|\mathbf{k}|}, \quad (\text{C2})$$

$$\text{and } \omega \sim \pm \frac{(\mathbf{B} \cdot \mathbf{k})^2}{2\boldsymbol{\Omega} \cdot \mathbf{k}} |\mathbf{k}|. \quad (\text{C3})$$

The modes corresponding to (C2) are inertial waves — in this context sometimes called “fast MC waves” — and those corresponding to (C3) are “slow MC waves”. By imposing magnetostrophic balance we neglect relative fluid accelerations, which corresponds to dropping the ω^2 term from the left-hand side of (C1). The dispersion relation then becomes

$$\omega = \pm \frac{(\mathbf{B} \cdot \mathbf{k})^2}{2\boldsymbol{\Omega} \cdot \mathbf{k}} |\mathbf{k}|, \quad (\text{C4})$$

so imposing magnetostrophic balance eliminates the two “fast” branches (C2) of the full dispersion relation (C1).

However, not all modes of the full dispersion relation (C1) have the asymptotic behavior described by (C2) and (C3). Even in the presence of rapid rotation, any mode for which $|\mathbf{B} \cdot \mathbf{k}| \rightarrow \infty$ fast enough that

$$|\mathbf{B} \cdot \mathbf{k}| \gg |2\boldsymbol{\Omega} \cdot \mathbf{k}| / |\mathbf{k}| \quad \text{as} \quad |\boldsymbol{\Omega}| \rightarrow \infty \quad (\text{C5})$$

behaves like an Alfvén wave, i.e., $\omega \sim \pm \mathbf{B} \cdot \mathbf{k}$. Imposing magnetostrophic balance removes the mechanism for Alfvén wave propagation, and must therefore alter the behavior of these modes. From (C4) we find that these modes now have a very high frequency. In fact if we fix $2\boldsymbol{\Omega} \cdot \mathbf{k}$ and allow $|\mathbf{k}| \rightarrow \infty$ then ω grows as $|\mathbf{k}|^3$. The conclusion is that even in a rapidly rotating system *some modes of the full dispersion relation always feel the Lorentz force more strongly than the Coriolis force*, and these modes become ill-behaved under the assumption of magnetostrophic balance. A numerical scheme that imposes magnetostrophic balance will therefore be ill-conditioned.

If we introduce stratification N^2 then (C4) becomes

$$\omega = \pm \frac{\mathbf{B} \cdot \mathbf{k}}{2\boldsymbol{\Omega} \cdot \mathbf{k}} [(\mathbf{B} \cdot \mathbf{k})^2 |\mathbf{k}|^2 + N^2 (|\mathbf{k}|^2 - k_V^2)]^{1/2}, \quad (\text{C6})$$

where k_V is the vertical component of \mathbf{k} . Therefore the presence of stratification serves only to increase the frequency of the ill-behaved modes, and thereby to exacerbate the problem.

REFERENCES

- Braithwaite, J., & Spruit, H. C. 2004, *Nature*, 431, L819
- Brun, A. S., & Zahn, J.-P. 2006, *A&A*, 457, 665
- Charbonneau, P., & MacGregor, K. B. 1993, *ApJ*, 417, 762
- Charbonnel, C., & Talon, S. 2007, in *Unsolved Problems in Stellar Physics*, ed. R. J. Stancliffe, J. Dewi, G. Houdek, R. G. Martin, and C. A. Tout, (Amer. Inst. of Physics, AIP Conf. Proc., vol. 948), 15-26
- Christensen-Dalsgaard, J., Proffitt, C. R., & Thompson, M. J. 1993, *ApJ*, 403, L75–L78
- Christensen-Dalsgaard, J., & Thompson, M. J. 2007, in *The Solar Tachocline*, ed. D. W. Hughes, R. Rosner, & N. O. Weiss (Cambridge: Cambridge University Press), 53
- Ciaccio, F., Degl’Innocenti S., & Ricci B. 1997, *A&A*, 123, 449
- Elliott, J. R. 1997, *A&A*, 327, 1222
- Elliott, J. R., & Gough, D. O. 1999, *ApJ*, 516, 475
- Garaud, P., & Brummell, N. H. 2008, *ApJ*, 674, 498
- Garaud, P., & Garaud, J.-D. 2008, *MNRAS*, 391, 1239–1258
- Gilman, P. A., & Cally, P. S. 2007, in *The Solar Tachocline*, ed. D. W. Hughes, R. Rosner, & N. O. Weiss (Cambridge: Cambridge University Press), 243
- Gough, D. O. 2007, in *The Solar Tachocline*, ed. D. W. Hughes, R. Rosner, & N. O. Weiss (Cambridge: Cambridge University Press), 3
- Gough, D. O., & McIntyre M. E. 1998, *Nature*, 394, 755
- Haynes, P. H., Marks, C. J., McIntyre, M. E., Shepherd, T. G., & Shine, K. P. 1991, *J. Atmos. Sci.*, 48, 651
- Kitchatinov, L. L., & Rüdiger, G. 2008, *Astron. Nachr.*, 329, 372
- McIntyre, M. E. 1994, in *The Solar Engine and its Influence on the Terrestrial Atmosphere and Climate* (Vol. 25 of NATO ASI Subseries I, Global Environmental Change, ed. E. Nesme-Ribes. Springer-Verlag, Heidelberg)
- McIntyre, M. E. 2007, in *The Solar Tachocline*, ed. D. W. Hughes, R. Rosner, & N. O. Weiss (Cambridge: Cambridge University Press), 183
- Mestel, L. 1953, *MNRAS*, 113, 716
- Mestel, L., & Moss D. 1986, *MNRAS*, 221, 25
- Mestel, L., & Weiss N. O. 1987, *MNRAS*, 226, 123
- Parfrey, K. P., & Menou, K. 2007, *ApJ*, 667, L207
- Press, W. H., Flannery, B. P., Teukolsky, S. A., & Vetterling, W. T. 1986, *Numerical Recipes: The Art of Scientific Computing*, (Cambridge: Cambridge University Press)
- Rogers, T. M., & Glatzmaier, G. A. 2006, *ApJ*, 653, 756
- Rüdiger, G., & Kitchatinov, L. L. 1997, *Astron. Nachr.*, 318, 273
- Schatzman, E. 1993, *A&A*, 279, 431
- Spiegel, E. A., & Zahn, J.-P. 1992, *A&A*, 265, 106
- Spruit, H. C. 2002, *A&A*, 381, 923
- Swenson, F. J., & Faulkner, J. 1992, *ApJ*, 395, 654–674
- Taylor, J. B. 1963, *Proc. R. Soc. Lond. A*, 274, 274–283
- Tobias, S. M., Brummell, N. H., Clune, T. L., & Toomre, J. 2001, *ApJ*, 549, 1183–1203
- Walker, M. R., Barenghi, C. F., & Jones, C. A. 1998, *GAFD*, 88, 261–275
- Weiss, N. O., Thomas, J. H., Brummell, N. H., & Tobias, S. M. 2004, *ApJ*, 600, 1073
- Wood, T. S. 2010, *The Solar Tachocline: A Self-Consistent Model of Magnetic Confinement*. PhD thesis, University of Cambridge Available from the Superintendent of Manuscripts, Cambridge University Library, West Rd, Cambridge CB3 9DR.

Wood, T. S., & McIntyre, M. E. 2007, in Unsolved Problems in Stellar Physics, ed. R. J. Stancliffe, J. Dewi, G. Houdek, R. G. Martin, and C. A. Tout, (Amer. Inst. of Physics, AIP Conf. Proc., vol. 948), 303. Corrigendum: see www.atm.damtp.cam.ac.uk/people/mem/papers/SQBO/solarfigure.html#chirality

Zahn, J.-P., Talon, S., & Matias, J. 1997, *A&A*, 322, 320